CrossMark

J. Fluid Mech. (2017), *vol.* 832, *pp.* 793–824. © Cambridge University Press 2017
doi:10.1017/jfm.2017.678

Lock-exchange release density currents over three-dimensional regular roughness elements

Kiran Bhaganagar[1],† **and Narasimha Rao Pillalamarri**[1]

[1]Laboratory of Turbulence, Sensing and Intelligence Systems, Department of Mechanical Engineering, University of Texas at San Antonio, San Antonio, TX 78249, USA

(Received 10 May 2017; revised 5 August 2017; accepted 17 September 2017; first published online 30 October 2017)

A fundamental study has been conducted to understand the front characteristics and the mixing in the flow of density currents over rough surfaces. A large-eddy simulation (LES) has been performed for lock-exchange release density currents over rough walls to shed light on the unsteady mixing processes. A volume-penalization method, which is a special case of the immersed-boundary method, has been implemented to realize the bottom-mounted rough topology. In this study, the LES has been conducted in a channel with a lower wall covered with three-dimensional cube- and pyramid-shaped roughness elements, such that all cases have the same base area, but differences in the roughness solidity and volume fraction of roughness. Both cases of identical roughness elements and those with randomness in height have been considered. The maximum roughness height for all cases is kept at a constant fraction (10 %) of the total channel height. The study focuses on the instantaneous mixing processes in lock-exchange release currents over rough surfaces. An important contribution of the work is that qualitative and quantitative analysis has been conducted to demonstrate additional mixing mechanisms due to the presence of surface roughness that enhances dilution of the current. Enhanced mixing due to roughness is related to the strength of the shear layer resulting from the roughness, and hence depends on friction Reynolds number (Re_τ). The combined role of current characteristics and Re_τ together dictate the mixing processes and extent of dilution in density currents over surface roughness.

Key words: gravity currents, topographic effects, turbulent mixing

1. Introduction

Three-dimensional (3D), turbulent, bottom-propagating density currents that arise due to the spreading of a heavier fluid into a lighter ambient fluid is of common occurrence in the atmosphere and in the oceans. These density currents play an important role in dictating atmospheric pollution, transport of airborne contaminants, ocean mixing and climate dynamics. The heavy fluid, as it propagates into the ambient fluid, entrains and mixes with the lighter ambient fluid, resulting in significant changes in the properties of the current. Knowledge of the front location, reduced gravity and

† Email address for correspondence: kiran.bhaganagar@utsa.edu

https://doi.org/10.1017/jfm.2017.678 Published online by Cambridge University Press

the dynamics of mixing are very important. The bottom surface on which these currents propagate is invariably rough in nature, and cannot be approximated as a smooth surface. More importantly, the type of roughness significantly influences the characteristics and dynamics of these 3D turbulent currents. Roughness introduces significant complexities in the physics, as well as the measurement techniques, and hence not much is understood of dense currents over roughness.

The problem considered in this research is the finite-volume release of a dense fluid into a lighter environment confined in a channel with rigid walls and a bottom wall covered with 3D regular roughness elements. This is the classical lock-exchange flow. The lock-exchange configuration has served as a canonical platform for both numerical and laboratory experiments to study gravity currents (Simpson 1972; Simpson & Britter 1979; Hacker, Linden & Dalziel 1996; Shin, Dalziel & Linden 2004; Özgökmen, Iliescu & Fischer 2009).

In a lock-exchange flow, a vertical barrier in a channel separates two fluids of different densities. The density difference between the heavy and lighter ambient fluids is small, and the Boussinesq approximation holds. Initially, the heavy fluid in the lock has stored potential energy, specified by the height of the lock. With the removal of the lock, the heavy lock fluid carrying the potential energy forms a well-defined frontal region after an initial transience. Beyond the short accelerating transient regime, the currents propagate with a constant velocity, referred to as the slumping regime (Britter & Simpson 1978; Rottman & Simpson 1983). The current moves horizontally, entraining the ambient fluid and growing spatially. From Benjamin's classical theory (Benjamin 1968), the most important characteristic feature of the current is the well-defined and distinctive head at the intruding end of the current, which is deeper than the rest of the current. The role of the head region in mixing processes has been clearly demonstrated by Simpson & Britter (1979). In lock-exchange flows, the head carries with it a fraction of the initial buoyancy in the lock, and this fraction is dictated by the lock aspect ratio (the ratio of the height to the length of the lock). At the top of the head region, strong Kelvin–Helmholtz (KH) billows form; these break down behind the head, causing strong mixing in the current, so that the interface becomes unstable towards the rear of the head. McElwaine's theory (McElwaine 2005) and particle image velocimetry measurements by Kneller, Bennett & McCaffrey (1999), Thomas, Dalziel & Marino (2003) and Samasiri & Woods (2015) indicate a strong mixing at the interface near the head of the current. Recently, Bhaganagar (2017) used large-eddy simulations (LES) to calculate mixing or entrainment coefficients as the fraction of the volume of the ambient fluid that enters the head due to shear instability generated at the current interface. An alternative way to quantify the entrainment in density currents is by using the concept of available potential energy introduced by Winters *et al.* (1995), and which has been successfully used to study the mixing processes (Prastowo *et al.* 2009; Hughes & Linden 2016; Micard *et al.* 2016).

Density currents over idealized smooth beds are well understood; however, the effect of bed roughness on the dynamics of lock-exchange currents needs clarification. Experimental and numerical data have contributed to our understanding of the effect of surface roughness on front characteristics (La Rocca *et al.* 2008; Özgökmen & Fischer 2008; Adduce *et al.* 2009; Tokyay, Constantinescu & Meiburg 2011; Nogueira *et al.* 2014; Yuksel Ozan, Constantinescu & Hogg 2015), detailed flow descriptions of the changes in the structure of the current as they interact with roughness (Gonzalez-Juez, Meiburg & Constantinescu 2009; Gonzalez-Juez *et al.* 2010; Bhaganagar 2014; Tokyay & Constantinescu 2015), time-averaged mixing

https://doi.org/10.1017/jfm.2017.678 Published online by Cambridge University Press

properties of the current (Negretti, Zhu & Jirka 2008; Tanino & Nepf 2008; Cenedese, Nokes & Hyatt 2017) and flow visualization studies (Peters & Venart 2000). In light of these previous studies, it is clear that surface roughness enhances the wall shear stress, and thus alters the flow characteristics in the frontal region. Density currents over rough surfaces have higher deceleration and faster dilution. Though the experimental studies have contributed to our understanding of the front velocity and structure of the current over roughness, unfortunately, not much knowledge is available on the temporal evolution of the currents and the mixing processes. In particular, it is not clear if the dilution occurs throughout the slumping regime or not.

In density currents, the primary source of mixing is the KH rollers, as the shear results in mixing at the interface. The question still remains as to how the wall shear generated near the roughness influences the primary mixing mechanisms. Furthermore, what is the contribution of the shear generated at the roughness elements in relation to the primary shearing mechanism at the interface? Field data collected by Fernandez & Imberger (2006) demonstrated that entrainment is mainly dependent on the stress generated at the bottom, directly determined by the roughness and the current properties. The effect of roughness on density current front evolution and mixing is very significant; however, our understanding on mixing in density currents over 3D roughness is still very limited. In particular, the instantaneous mixing process during the slumping regime is still not clear, and the role of local roughness features in diluting the current has not been quantified.

The effect of surface roughness on the flow is very complicated, as roughness geometrical metrics including roughness height, shape and distribution influence the near-wall flow dynamics. In the near-wall region of turbulent flows, as viscosity is important, the relevant velocity scale is the friction velocity $u_\tau = \sqrt{\tau_w/\rho}$. For wall-bounded, constant-density turbulent flows, high-resolution numerical and experimental studies quantified the role of wall shear stress due to uniform and irregular blocks of roughness in terms of u_τ (Bhaganagar, Kim & Coleman 2004; Wu & Christensen 2010; Bhaganagar & Chau 2015). Similarly, the near-wall region of the density current has a significant role in modifying the flow dynamics, and in particular the wall shear stress (τ_w), which manifests itself as a mean velocity gradient at the wall and dictates the frictional drag encountered by the current. The local Reynolds number based on the friction velocity can be defined as $Re_\tau = u_\tau h_H/\nu$, based on local current height (h_H). In this study, we characterize the instantaneous wall shear stress in terms of Re_τ. There is evidence that enhanced wall shear stress dilutes the current and manifests as enhanced entrainment. High-resolution LES were used by Tokyay, Constantinescu & Meiburg (2012) to demonstrate that two-dimensional (2D) dunes entrain higher than 2D ribs of comparable size and relate the time evolution of u_τ to entrainment.

The early works of Nikuradse (1933) and the classical experiments of Schlichting (1936) used roughness height and the spacing between the roughness elements to classify roughness. Recent experimental (Schultz & Flack 2009; Wu & Christensen 2010) and numerical data (Orlandi & Leonardi 2006; Chau & Bhaganagar 2012; De Marchis & Napoli 2012) on constant-density turbulent flows over roughness revealed new insights on roughness parameters that influence the wall shear stress. Roughness volume fraction (the ratio of the volume occupied by roughness to the volume of the surrounding fluid) and roughness solidity (the ratio of the total frontal area of the roughness in relation to the base area) have emerged as reliable metrics to quantify the wall shear stress due to roughness geometry (Lettau 1969; Counehan 1971; Macdonald, Griffiths & Hall 1998; Flack & Schultz 2014). Hence, in this study,

https://doi.org/10.1017/jfm.2017.678 Published online by Cambridge University Press

the density currents are studied within the context of roughness solidity and volume fraction.

Only in the recent literature have data on instantaneous entrainment started to appear. Analysis of density currents over smooth surfaces from experimental measurements and high-resolution LES studies (e.g. Ottolenghi *et al.* 2016; Bhaganagar 2017) have revealed that entrainment is a highly unsteady process and dilution of the current starts as early as the beginning of the slumping regime. Fragoso, Patterson & Wettlaufer (2013) used highly spatially resolved optical based experiments to study the temporal entrainment during the slumping regime, and provided some of the first evidence that mixing in the head of a density current starts during the early stages of the slumping regime. Data on density currents over rough surfaces is even more sparse. The few available data for the current over surface roughness include the experimental data by Wilson, Friedrich & Stevens (2017) for isolated roughness and by Nogueira *et al.* (2014) for a sediment bed. In the latter study, the temporal evolution of current depth-averaged density was analysed to demonstrate roughness results in significant dilution during the beginning of the slumping regime. The present investigation is one of the first studies to use highly resolved data to explore the instantaneous mixing processes in the density current over 3D roughness elements. We focus on 3D regular roughness elements, including cubes, pyramids, combinations of cubes and pyramids consisting of both cases with identical roughness elements and with elements consisting of random height distribution. The maximum height of the roughness elements is 10 % of the lock height, and the elements are well immersed within the current.

In this paper, the following research questions will be addressed.

(i) For the same initial conditions of the lock, what are the differences in the front characteristics over a rough wall compared to a smooth wall? In particular, what are the differences that arise due to difference in roughness shape (i.e. cubes versus pyramid shape), and what are the differences that arise due to difference in identical versus random arrangement of roughness elements with the same mean height of roughness and centre–centre spacing between the roughness elements? Differences in cubes/pyramids and uniform/random height introduce differences in roughness metrics, such as volume fraction of roughness and area ratio of roughness.

(ii) How does roughness affect the instantaneous mixing in the density current? How does the instantaneous entrainment and mixing during the slumping and inertial regimes of density currents depend on the roughness? This is connected to an understanding of the role of wall shear stress versus the shear at the interface due to KH instability that contributes to entrainment of ambient fluid into the current. This is also related to the question: Is the modified flow dynamics and the consequences of mixing due to the differences in the roughness configuration represented by friction Reynolds number (Re_τ)?

The paper is arranged as follows. The physical problem with the simulation domain and the boundary conditions considered in this analysis is presented in § 2.1. We use a finite-volume LES methodology with a Boussinesq approximation to solve the 3D nonlinear Navier–Stokes (NS) momentum equations and scalar transport equation. The subgrid scales are modelled using the dynamic Smagorinsky eddy viscosity model. Roughness is introduced using a penalization approach by solving the Darcy–Brinkman equation, where, in the limiting case of permeability approaching zero/infinity, the domain mimics solid/fluid regions. The details of the NS formulation

https://doi.org/10.1017/jfm.2017.678 Published online by Cambridge University Press

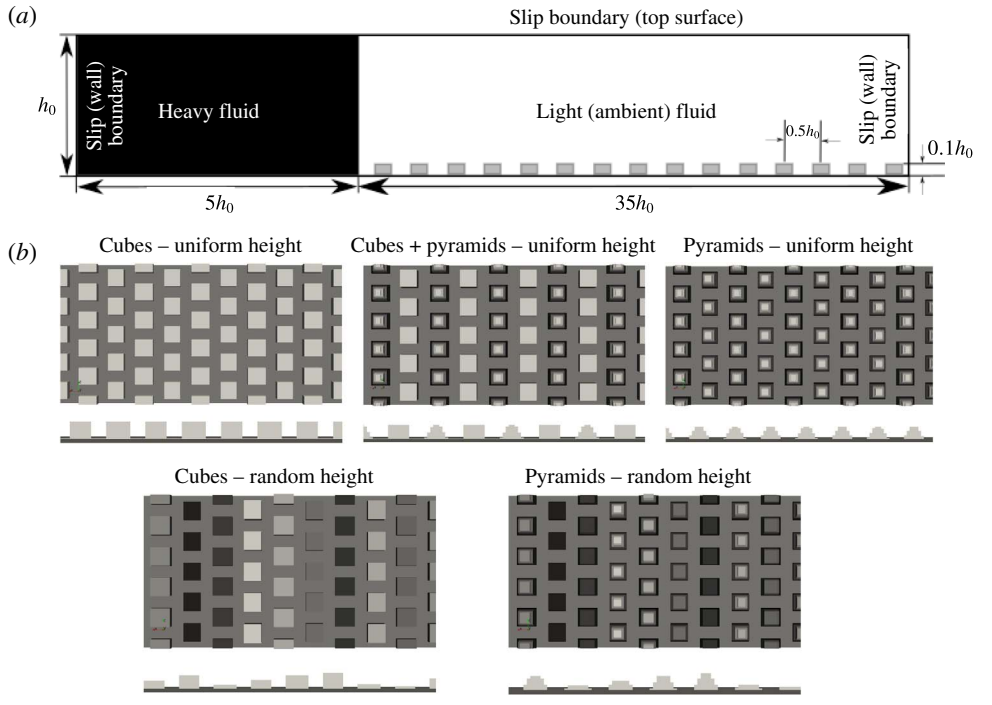


FIGURE 1. (*a*) Schematic of the computational domain for lock-exchange release system with lock of height h_0 and length $5h_0$. The roughness elements are placed on the lower wall of the channel. (*b*) The five rough-wall cases that are considered in this work. The roughness elements comprise cubes, pyramids and combinations of cubes and pyramids of uniform elevation (top row), and cubes and pyramids with random elevation (bottom row). For all the cases the mean roughness height is $0.1h_0$.

and the approach to mimic the roughness are explained in §§ 2.2 and 2.3, respectively. The front characteristics and the definitions to quantify the current are explained in § 2.4. The results are presented in § 3, flow regimes and the associated analysis is discussed in §§ 3.1–3.4, shear stress results are discussed in § 3.5, and finally the entrainment and mixing are discussed in § 3.6. In § 4, we present the conclusions.

2. Problem formulation and numerical approach

2.1. *Simulation domain and boundary conditions*

The physical problem considered is a horizontal channel with the lower wall dotted by bottom-mounted roughness elements; the upper wall is a fixed rigid wall, as shown in figure 1(*a*). The problem at hand is a full lock release case, where the lock height is the same as the height of the channel (h_0). Initially, the heavy fluid fills the lock of length L_0 ($L_0 = 5h_0$). The lock aspect ratio (L_0/h_0) is 5. The streamwise and spanwise extents of the domain are $40h_0$ and $2.5h_0$, respectively. In this work, the rough wall consists of 3D regular roughness elements with a fixed distribution of roughness features that are in the shapes of cubes and pyramids having uniform and random heights. We will refer to the distribution of roughness with uniform elevation as uniform roughness, and the distribution with random elevations as random roughness. Figure 1(*b*) shows the top and front views for the different cases that are considered

https://doi.org/10.1017/jfm.2017.678 Published online by Cambridge University Press

in this study. The cases consist of identical cube-shaped roughness elements that are referred to as 'uniform cubes', identical pyramid-shaped roughness elements that are called 'uniform pyramids', combinations of both cubes and pyramids of uniform height, which are referred to as 'uniform cubes and pyramids', cubes with random height distribution referred to as 'random cubes', and pyramids with random height distribution referred to as 'random pyramids'. Definitions of roughness metrics, listed in table 1, include the following.

(i) Volume fraction (V_f),

$$V_f = \frac{\sum_{i=1}^{390} V_i^R}{V_0}, \tag{2.1}$$

where V_i^R is the volume of the ith roughness feature and V_0 is the volume of the simulation domain.

(ii) Surface fraction (S_f),

$$S_f = \frac{A_i^R}{A_b}, \tag{2.2}$$

where A_i^R is the total surface area of the ith roughness feature and A_b is the area of unoccupied bottom bed. Surface fraction (S_f) is unique for each case and exercises a direct influence on bottom shear experienced by the advancing current.

(iii) Streamwise solidity (Γ_1),

$$\Gamma_1 = \frac{A_j^P}{l_{span} h_0}, \tag{2.3}$$

where A_j^P is the area of the jth row of roughness features when projected on the right (slip) wall of the domain, h_0 is the channel height and l_{span} is the length of the span. Thus Γ_1 represents the solidity (Schlichting 1936; Jimenez 2004; Flack & Schultz 2014) normal to the channel span. It is constant when roughness shapes and heights remain unchanged (cases 4 and 6) but fluctuates with variation in either one of them (cases 2, 3 and 5). Therefore, we present the maximum $(\Gamma_1)_{max}$, mean $(\Gamma_1)_{mean}$ and minimum $(\Gamma_1)_{min}$ values for Γ_1. The zero entries for $(\Gamma_1)_{min}$ in cases 1 and 2 convey that randomness in the feature heights lead to a smooth surface in certain stretches of the bottom wall.

(iv) Spanwise solidity (Γ_2),

$$\Gamma_2 = \frac{\sum_{j=1}^{78} A_j^S}{L h_0}, \tag{2.4}$$

where A_j^S is the area of the jth row of roughness features when projected on the front (periodic) boundary of the domain. Thus Γ_2 represents solidity normal to the channel length ($L = 40h_0$). Like S_f, Γ_2 is constant and unique for each roughness case.

The case studies considered have the same maximum roughness height (k), streamwise spacing $\lambda_x = 5k$ and spanwise spacing $\lambda_z = 5k$ between the roughness elements. The maximum roughness height is the same for all cases, and is considered to be 10 % of the lock height. The volume fraction is different for each case, and

https://doi.org/10.1017/jfm.2017.678 Published online by Cambridge University Press

Case	Shape	Elevation	V_f (%)	S_f	$(\Gamma_1)_{max}$	$(\Gamma_1)_{mean}$	$(\Gamma_1)_{min}$	Γ_2
1 (SB)	Smooth bed	—	—	—	—	—	—	—
2 (PR)	Pyramids	Random	1.19	0.79	0.04	0.025	0	0.025
3 (CR)	Cubes	Random	1.94	0.913	0.06	0.033	0	0.032
4 (PU)	Pyramids	Uniform	1.63	0.983	0.04	0.04	0.04	0.038
5 (CPU)	Cubes + Pyramids	Uniform	2.56	1.12	0.06	0.05	0.04	0.048
6 (CU)	Cubes	Uniform	3.51	1.262	0.06	0.06	0.06	0.058

TABLE 1. Characteristics of roughness distribution and shape. For definitions of V_f, S_f, Γ_1 and Γ_2 refer to (2.1)–(2.4), respectively.

it varies from the greatest for uniform cubes (3.51 %) to the smallest (1.19 %) for pyramids with random roughness. All cases have the same ratio of the total plan area of the obstacles to the lower wall area. The cases have different ratios of the total frontal area of the obstacles to the total area, because, though the cases with uniform pyramids and cubes have the same plan area, roughness height and spacing between the obstacles, the obstacles have different total frontal areas. The differences between the uniform cubes versus the random cubes or uniform pyramids versus random pyramids is the difference in variation of solidity. The case with combination of uniform cubes and pyramids has a different total frontal area and solidity.

2.2. *Governing equations*

A finite-volume LES implementation, with penalization-function-type immersed-boundary method to realize the bottom mounted obstacle geometry, has been used to simulate turbulent density currents. The governing equations are the following filtered NS system of equations, under Boussinesq approximation (filtered variables are denoted by overbar).

(i) Continuity equation:

$$\boldsymbol{\nabla}\cdot\overline{\boldsymbol{u}}=0. \tag{2.5}$$

(ii) Momentum equation:

$$\frac{\partial\overline{\boldsymbol{u}}}{\partial t}+\overline{\boldsymbol{u}}\cdot\boldsymbol{\nabla}\overline{\boldsymbol{u}}=-\frac{\boldsymbol{\nabla}\overline{p}}{\rho}+\nu\nabla^2\overline{\boldsymbol{u}}+\boldsymbol{\nabla}\cdot\{(\nu+\nu_t)[\boldsymbol{\nabla}\overline{\boldsymbol{u}}+(\overline{\boldsymbol{u}})^{\mathrm{T}}]\}+\overline{\rho}\boldsymbol{g}+\overline{\boldsymbol{f}}, \tag{2.6}$$

where $\overline{\rho}$ represents the resolved relative density field and $\overline{\boldsymbol{f}}$ is a source term, which will be discussed in detail in § 2.3. The third term on the right-hand side results from applying the spatial filter to the convection term in the NS equation and invoking the Boussinesq hypothesis of a linear stress–strain relationship. Finally, ν_t represents the eddy viscosity, which is calculated from the dynamic Smagorinsky model proposed by Germano *et al.* (1991).

(iii) Transport equation:

$$\frac{\partial\overline{\rho}}{\partial t}+\boldsymbol{\nabla}(\overline{\rho}\overline{\boldsymbol{u}_j})=\boldsymbol{\nabla}(\kappa_{eff}\boldsymbol{\nabla}\overline{\rho}), \tag{2.7}$$

where $\kappa_{eff}=\nu_t/Sc_t+\nu_0/Sc$.

https://doi.org/10.1017/jfm.2017.678 Published online by Cambridge University Press

The solver executes the 'pressure-implicit with splitting of operators' (PISO) algorithm to evaluate the momentum flux. PISO decouples the pressure and velocity fields by splitting the operators into implicit predictor and multiple explicit corrector steps. Furthermore, the convective term is linearized by using the convective velocity from the previous time step. Time integration is undertaken using a second-order-accurate bounded three-point backward scheme. Convective terms are handled with a bounded Gauss self-filtered central difference (SFCD) scheme, diffusion terms are handled using a Gauss scheme with linear interpolation, and scalar transport is calculated using a Gauss–Vanleer scheme.

2.3. *Penalization method*

A volume-penalization-based immersed-boundary method is used to realize the roughness topology on a pure Cartesian mesh. This approach is a special case of feedback forcing procedure (Goldstein, Handler & Sirovich 1993); however, here the solid regions are manifested as a porous medium with vanishing permeability (Angot, Bruneau & Fabrie 1999). The fields in the time-discretized momentum equation are replaced with penalized quantities $\boldsymbol{u}_\eta$ and p_η such that $\boldsymbol{u}_\eta = \overline{\boldsymbol{u}} + \eta\widetilde{\boldsymbol{u}}$ and $p_\eta = \overline{p} + \eta\widetilde{p}$. The symbol η represents the penalization parameter ($\eta \ll 1$). Therefore, as $\eta \to 0$, the penalized velocity field $\boldsymbol{u}_\eta \to \overline{\boldsymbol{u}}$ and error $\widetilde{\boldsymbol{u}} \to 0$:

$$\frac{\partial \boldsymbol{u}_\eta}{\partial t} + \boldsymbol{u}_\eta \cdot \boldsymbol{\nabla}\boldsymbol{u}_\eta = -\frac{\boldsymbol{\nabla} p_\eta}{\rho} + \nu\nabla^2\boldsymbol{u}_\eta + \boldsymbol{\nabla}\cdot\{(\nu+\nu_t)[\boldsymbol{\nabla}\boldsymbol{u}_\eta + (\boldsymbol{\nabla}\boldsymbol{u}_\eta)^{\mathrm{T}}]\} + \overline{\rho}\boldsymbol{g} - \frac{\chi}{\eta}\boldsymbol{u}_\eta + \overline{\boldsymbol{f}}. \tag{2.8}$$

Equation (2.8) is defined over a heterogeneous domain (Ω) comprising fluid region Ω_f and solid region Ω_s such that $\Omega_f \cup \Omega_s = \Omega$ and $\Omega_f \cap \Omega_s = \emptyset$. The boundary between Ω_f and Ω_s is denoted by Γ. The second last term in (2.8) is introduced into momentum equation (2.6) to account for the heterogeneous nature of the domain; here χ represents a masking function that distinguishes solid and fluid regions,

$$\chi = 0 \quad \forall \boldsymbol{x} \in \Omega_f, \tag{2.9}$$

$$\chi = 1 \quad \forall \boldsymbol{x} \in \Omega_s. \tag{2.10}$$

Substituting the definitions of $\boldsymbol{u}_\eta$ and p_η in (2.8) and identifying terms of the same order, for Ω_s, leaves us with

$$\frac{\boldsymbol{\nabla}\overline{p}}{\rho} + \frac{\boldsymbol{u}_\eta - \overline{\boldsymbol{u}}}{\eta} + \overline{\rho}\boldsymbol{g} = \overline{\boldsymbol{f}} \quad \forall \boldsymbol{x} \in \Omega_s. \tag{2.11}$$

Therefore, if Ω_s is interpreted as a porous medium, given that no additional external force is active (i.e. $\overline{\boldsymbol{f}} = 0$ and $\overline{\rho}\boldsymbol{g} = 0$), the penalization parameter (η) will correspond to its permeability (K). Furthermore, as $\eta \to 0$ the permeability of the porous medium will diminish; asymptotically we realize a rigid solid. A similar analysis for (Ω_f) retrieves the momentum equation in its native form (2.6). Angot *et al.* (1999) conveyed that *a priori* estimation of penalized velocity, subject to an incompressibility constraint, results in a penalized velocity field ($\boldsymbol{u}_\eta$) that converges towards fluid velocity ($\boldsymbol{u}$) as $\eta \to 0$. In numerical simulations this estimation can be passed as initial conditions to the solver. Introducing the velocity term of Darcy's equation (an empirical relation governing flows through porous media) as a forcing term coupled with masking function χ in the momentum equation allows the forcing to vanish in the fluid region ($\chi = 0$) and activate only within the solid region ($\chi = 1$). The forcing

https://doi.org/10.1017/jfm.2017.678 Published online by Cambridge University Press

term introduces excessive volumetric drag on account of $K \to 0$, thus bringing momentum flux across the solid region down to machine precision. Consequently, the convection terms cease to influence the momentum transport. Left with time derivative, diffusion term, pressure gradient and the forcing term (in the form of Darcy's law), we realize Brinkman's (1949) formulation for simulating flow through a porous medium.

Cases reported in this work comprise roughness features in the shape of cubes and stepped pyramids. At this point focus is laid on geometric simplicity, so both shapes mentioned above can be realized by simply combining orthogonal hexahedral control volumes in sequential arrays. Each feature thus comprises an integer multiple of control volume cells. The control volumes comprising roughness features are referenced in a cell-zone data structure and passed on to the solver. For these control volumes the solver assigns $\chi = 1$ while evaluating momentum flux. The forcing term emulates the left-hand side of Darcy's law. To accommodate higher Reynolds numbers, the Forchheimer correction (Forchheimer 1901) has been applied to Darcy's law. Therefore,

$$\bar{\boldsymbol{f}} = -\left[\mu \boldsymbol{D} + \tfrac{1}{2}\rho|\overline{\boldsymbol{u}}|\boldsymbol{F}\right]\overline{\boldsymbol{u}}, \tag{2.12}$$

where $\boldsymbol{D} = 1/K_{ij}$ and $\boldsymbol{F} = 2C_E/\sqrt{K_{ij}}$. The permeability tensor K_{ij} is a free parameter specified by the user; under the isotropic assumption it transforms to a constant scalar and consequently D_{ij} and F_{ij} also manifest as constant scalars. Ergun's constant C_E (Ergun 1952) is derived from empirical relations. For our problem formulation, we directly define D and F to be of the order of 10^{20}. This number is arrived at after conducting sensitivity tests; at this order and beyond, the volume-averaged velocity within the porous medium is recorded to be of the order of 10^{-12}, which is close to machine precision and therefore inconsequential.

2.4. *Front characteristics*

The density current is bounded by a strong frontal region called the 'head' of the current. The shallower current following will be referred to as the 'tail' of the current (Simpson 1982). The two characteristic length scales of the density current are the current depth of the head (h_H) and the depth of the tail (h_t). The leading edge, or the foremost point of the current, is identified as the front (x_f), and the time rate of change of the streamwise location of this point is referred to as the front velocity (u_f). A key quantity of interest is the non-dimensional u_f, which is based on the characteristic current depth and reduced gravity. The non-dimensional parameter, Froude number (Fr), will identify the regime of the density current. As most of the mixing in the density current is in the active 'head' region of the current, it is equally important to obtain a characteristic measure of the available buoyancy in the head.

The depth of the current is unsteady and is not clearly defined. One of the uncertainties in accuracy of measurements of entrainment and mixing in density currents is the identification of the interface between the current and the ambient fluid. A commonly used method to identify the current depth is the threshold criterion (e.g. Härtel, Meiburg & Necker 2000; Cantero *et al.* 2006), which is defined as the height at which the density reaches a prescribed threshold (e.g. 5 % or 10 % that of the lock fluid). This method is sensitive to the threshold selected, especially due to the presence of KH billows resulting in overestimation of the depth at locations corresponding to KH rollers. This definition introduces an uncertainty when calculating depth from instantaneous fields due to intermittent mixing of ambient fluid into the current. As a note, a commonly used alternative method is an integral approach (Shin *et al.*

https://doi.org/10.1017/jfm.2017.678 Published online by Cambridge University Press

2004), which is based on local buoyancy, and is defined as $\overline{h(x,t)} = \overline{g'h(x,t)}/g'_0$, where $\overline{g'h(x,t)} = g\int_0^{h_0}[(\rho(y)-\rho_L)/\rho_H]\,\mathrm{d}y$ (ρ_H and ρ_L represent the densities of the heavy and the light fluids, respectively). In both of these methods, the head height is defined as the maximum value of $h(x,t)$ over x (e.g. Ottolenghi *et al.* 2016). We adopt a method that is free from the uncertainty of the threshold criterion, and which is based on potential energy criteria developed by Anjum, McElwaine & Caulfield (2013). This method is a robust method, not only to define the depth of the current but also to identify the location of the head in terms of its available potential energy. The method has been implemented successfully by Borden & Meiburg (2013) and Zgheib, Bonometti & Balachandar (2015), and it captures the head of the current and regions corresponding to breakdown of KH billows more accurately. The methodology to capture the front interface and the head height is described next.

2.4.1. *Methodology for identification of front interface*

The spanwise-averaged density field, $\rho(x,y,t)$, is calculated at each time instant, and the maximum density at each stream-wise location x and for each time t along the current is determined as

$$\rho_m(x,t) = \max_y(\rho(x,y,t)). \tag{2.13}$$

For each x that is within the current, ρ_m is the maximum at x where there is only unmixed lock fluid, and it sharply decreases to the minimum at the front interface between the current and the ambient fluid that is ahead of the current. The inflection point along this curve is the location of the front (x_f). From Benjamin's (1968) theory, the curvature of the current switches from being negative near the nose to being positive above the nose; hence the inflection point of the maximum density (which always occurs closer to the lower wall) is an unambiguous way of obtaining the front location. The main advantage of this method is that there is no need to specify a density threshold value to identify the front location. We fit a cubic spline through the data and obtain an inflection point of the fitted function. Figure 2 shows an illustration of ρ_m versus x plotted at $t = 50$ s after the release of the gate. The cross sign marks the inflection point. Also shown in figure 2 is the 2D field of spanwise-averaged density at this corresponding time. The method captures the foremost point of the density current. The front speed (u_f) is defined as the rate of change of x_f, which has been calculated using (2.13).

2.4.2. *Methodology for calculation of head height*

In the potential energy method, the instantaneous depth of the current, which is the interface between the current and the ambient fluid, is defined as

$$h(x,t) = 2\frac{\displaystyle\int_0^{h_0}[\rho(x,y,t)-\rho_L]y\,\mathrm{d}y}{\displaystyle\int_0^{h_0}[\rho(x,y,t)-\rho_L]\,\mathrm{d}y}, \tag{2.14}$$

where ρ_L is the density of the ambient fluid. The first maximum from the leading edge of $h(x,t)$ is defined as the height of the head, h_H,

$$h_H = h(x^*,t), \quad \text{where } x^* = \max\left\{x:\left(\frac{\mathrm{d}h_f}{\mathrm{d}x^*}\right)_{x=x^*} = 0\right\}. \tag{2.15}$$

https://doi.org/10.1017/jfm.2017.678 Published online by Cambridge University Press

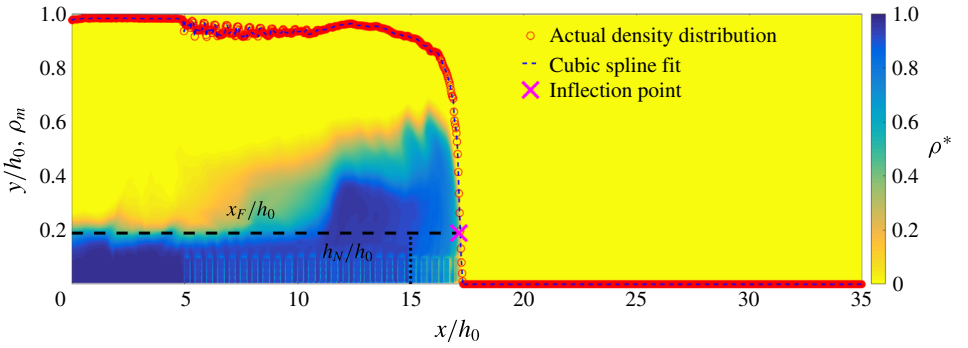


FIGURE 2. (Colour online) The spanwise-averaged non-dimensional density field, $\rho^* = (\rho_{xy} - \rho_L)/(\rho_H - \rho_L)$ for current advancing over uniform cubes. The subscript xy refer to the 2D spatial location. Subscripts H and L identify the heavy and ambient fluids, respectively. Superimposed is the maximum density (ρ_m) at each streamwise location at $t = 50$ s ($\rho_m = \max_y[\rho^*(x, y, t)]$).

3. Results

Six lock-exchange release experiments were performed for the cases shown in table 1. The simulations were conducted in a channel of length $L = 4$ m and height $h_0 = 0.1$ m with a span $b = 0.25$ m. The same initial conditions were used for all cases, with an initial reduced gravity of $g_0' = 0.05$. The driving force, or equivalent pressure gradient, was the initial buoyancy in the lock, $B_0 = g_0' L h_0 b$. Case 1 corresponds to a density current over smooth walls, and cases 2–6 correspond to density currents over rough walls. We begin our analysis by examining the front conditions.

3.1. *Front regimes*

The front position scales with the lock length $(x_f - L_0)/L_0$ versus non-dimensional time t/t_0, where $t_0 = h_0/\sqrt{g_0' h_0}$, as shown in figure 3(*a*). The front over the smooth wall with no roughness moves with a constant velocity, and hence the slope in the x–t plot is unity, indicating that the current is in the slumping regime. The experimental results of Huppert & Simpson (1980) have clearly demonstrated that lock-exchange release density currents go through different well-defined regimes: slumping regime, in which buoyancy is constant, followed by an inertial regime, where the buoyancy forces are balanced by the inertial forces, resulting in $x_f \propto t^{2/3}$. For the present case, the current over the smooth wall is in the slumping regime until the end of the simulation. Differences in the slopes and regimes are evident for the rough-wall cases. Two distinct regimes are evident for the rough-wall cases. In the initial regime, the slope of the trajectory in the x–t plane varies with roughness and it is not constant in this regime but is within the following range: it is 0.92–0.99 for uniform cubes; 0.92–0.97 for the combination of uniform cubes and pyramids; 0.94–0.97 for uniform pyramids; 0.9–0.98 for the random cubes; and 0.93–0.99 for the random pyramids. As the slope is nearly 1, this regime can be well approximated as the slumping regime. It should be noted that, during the slumping regime over the rough wall, the presence of the spatial inhomogeneity in the vicinity of the roughness causes the large-amplitude temporal variation in the front velocity, resulting in varying slope within this regime. Hence, the variation of the slope is much higher for the random

https://doi.org/10.1017/jfm.2017.678 Published online by Cambridge University Press

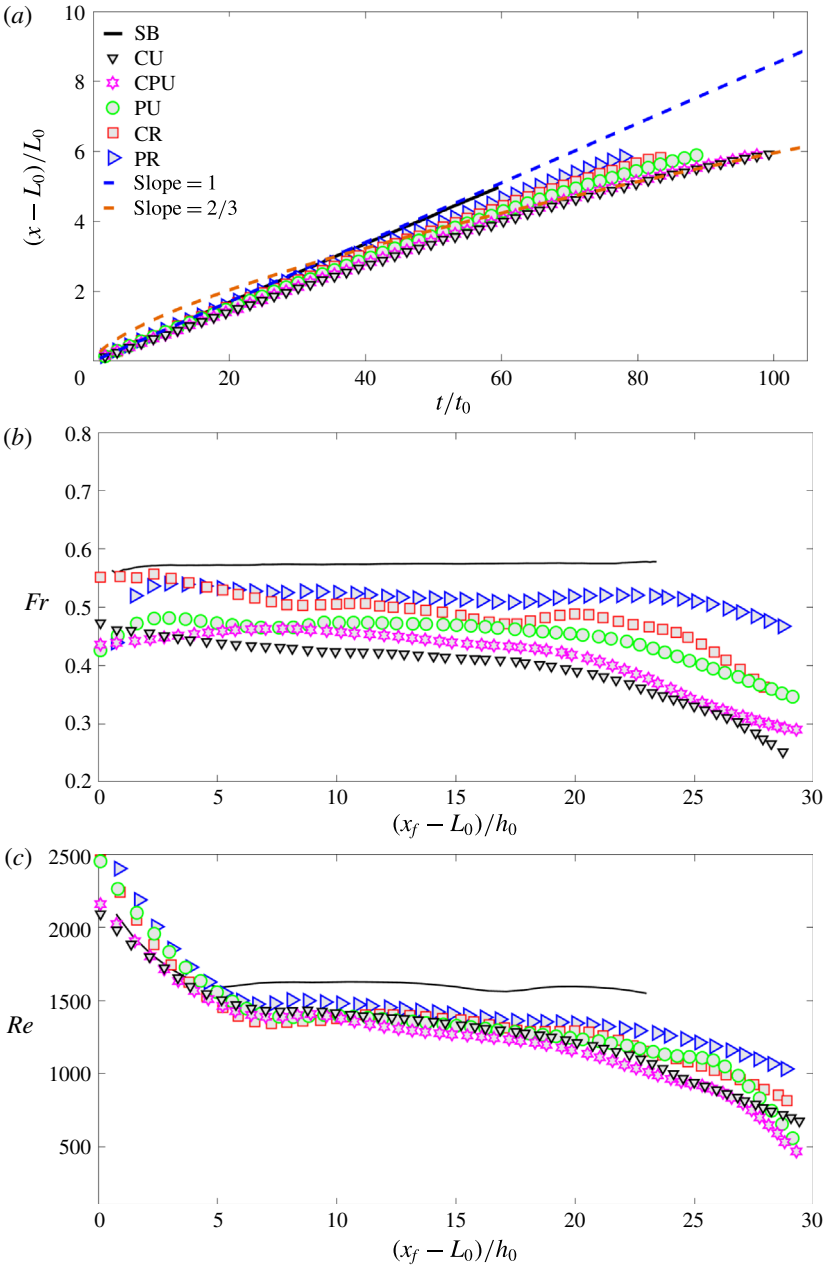


FIGURE 3. (Colour online) (*a*) Front location x_f scaled with lock length versus non-dimensional time. See table 1 for details of the initials listed in the key. Also shown are the lines with constant slope of 1 and 2/3. (*b*) Froude number $Fr = u_f/(\sqrt{g_0' h_H})$ versus non-dimensional front location. Symbols as in panel (*a*). (*c*) Reynolds number $Re = (u_f h_H)/\nu$ versus non-dimensional front location. Symbols as in panel (*a*).

roughness cases compared to uniform roughness case. All the rough-wall cases show a transition from the slumping regime, where the slope changes suddenly, and current begins to slow down. The slope in this regime varies from 0.65 to 0.7, depending

https://doi.org/10.1017/jfm.2017.678 Published online by Cambridge University Press

on the roughness type. At this time the current has entered the inertial regime. The analytic model of Tanino, Nepf & Kulis (2005) predicts a slope of 0.67, where $x_f \propto t^{0.67}$ when the current is in the inertial regime. The slope obtained from the numerics is a close match to that predicted by theory. These results serve as a robust validation and confirm the presence of well-defined regimes for the density currents. They are consistent with the existence of the regimes from the theoretical study of Fay (1969) and substantiated by experiments (Fannelop & Waldman 1971; Hoult 1972).

3.2. *Characteristic non-dimensional measures of the density currents*

The non-dimensional numbers that characterize the state of density currents are the Froude number (Fr) and the Reynolds number (Re). The Froude number reflects the transition of the potential energy available in the form of a heavy fluid into the kinetic energy of the propagating current, and it is defined as $Fr = u_f/\sqrt{g'_0 h_H}$, where u_f is the front velocity and initial reduced gravity is $g'_0 = g(\rho_H - \rho_L)/\rho_L$ (ρ_H represents density of the undiluted heavy fluid and ρ_L represents density of the ambient fluid). The Reynolds number is defined as $Re = u_f h_H/\nu$. It should be noted that Re is based on the local front velocity and the maximum depth of the current in the head region. Figure 3(*b*) shows the Froude number Fr versus non-dimensional front location; the front over the smooth wall moves with a constant velocity of $Fr = 0.56$ in the slumping regime. Roughness slows down the front due to enhanced drag, and Fr decreases with roughness, with lowest value for uniform cubes, followed by uniform cubes and pyramids, uniform pyramids, random cubes and finally random pyramids. From this trend, Fr decreases with increasing spanwise solidity Γ_1. This is reasonable as the drag encountered by the front (leading edge of the current) depends on the ratio of the blockage due to roughness with respect to the cross-sectional area at that location. Hence, it is expected that Fr shows a dependence on the spanwise solidity and this is consistent with theory. In the slumping regime, the mean Fr varies from 0.42 to 0.52 for roughness cases. This result is consistent with the experiments of Keulegan (1958) and Barr (1963). Figure 3(*c*) shows the Re versus non-dimensional front location. Here, Re represents the local state of the current, as it is based on local velocity and length scales. As expected, the rough-wall cases have lower values of Re than the smooth-wall example. However, it is interesting that for all the roughness cases the variation of Re is in the range of 1290–1420 in the slumping regime, whereas deviation starts to appear towards the beginning of the inertial regime. We will explore this further when we discuss the mixing mechanisms.

Overall, it is clear that the current over the smooth wall is in the slumping regime throughout the simulation. The presence of roughness alters the behaviour of the front. As the solidity of roughness increases, the front travels with slower velocity in the slumping regime, and it transitions to the inertial regime much faster due to enhanced drag. When the front passes over the roughness elements, the spatial inhomogeneity in the vicinity of roughness causes high temporal variations in the data. Similar trends have been observed by Tokyay *et al.* (2011) for 2D ribs; they noted that, as the front passed the crest and then the valley of the roughness, there was an increase in the potential energy and loss in kinetic energy at the crest, followed by a decrease in potential energy at the valley, and thus the front encountered sudden deceleration and acceleration as it passed through each roughness element. This results in large temporal variations in the front velocity.

https://doi.org/10.1017/jfm.2017.678 Published online by Cambridge University Press

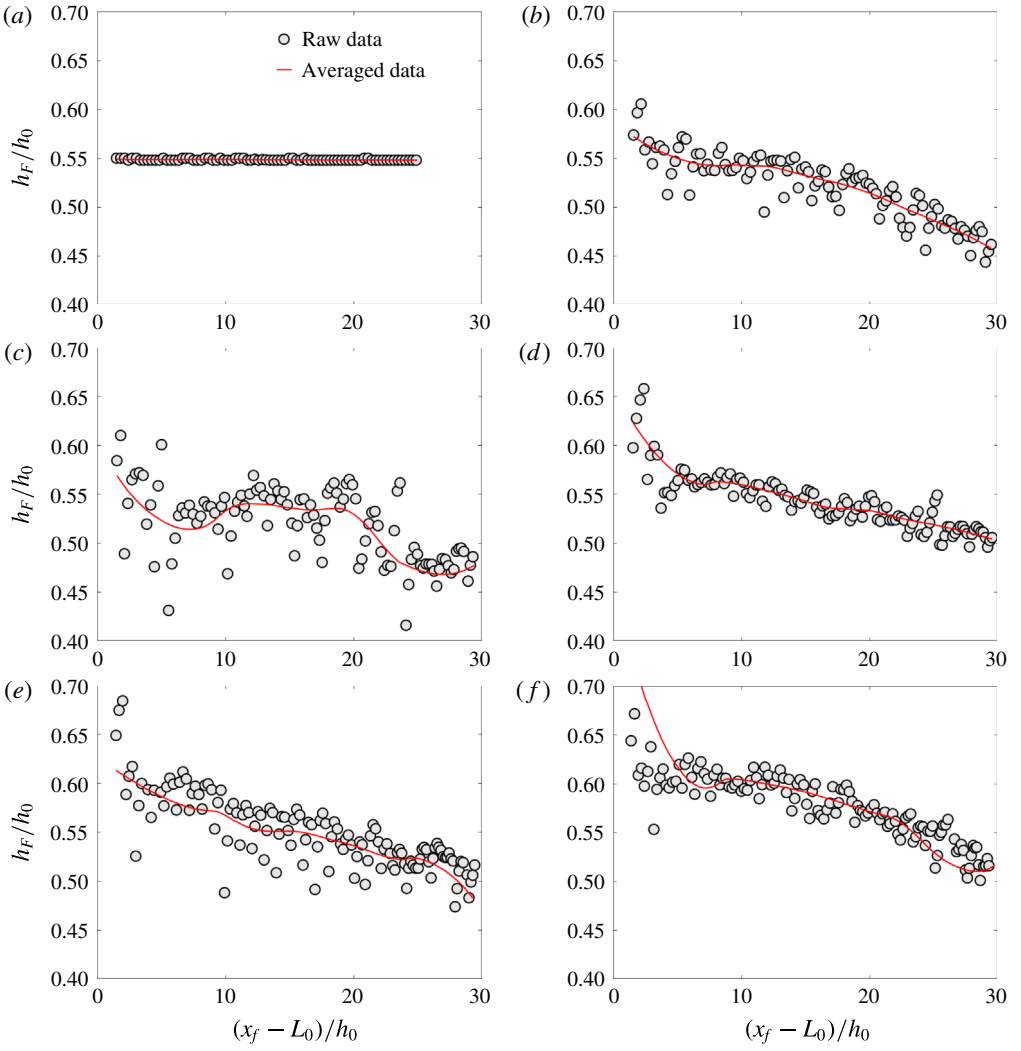


FIGURE 4. (Colour online) Variation in head height of advancing current: (*a*) smooth bed (SB), (*b*) pyramids with random height (PR), (*c*) cubes with random height (CR), (*d*) pyramids with uniform height (PU), (*e*) cubes and pyramids with uniform height (CPU), and (*f*) cubes with uniform height (CU).

3.3. *Investigation of roughness metrics on current depth and head height*

The depth of the instantaneous head location calculated using (2.15) is referred to as the head height. The variation of the head height as the front advances forwards is shown in figure 4. The importance of head height is that the higher the depth of the current, the higher the amount of volume of entrained fluid, and thus the greater the enhanced mixing in the current. During the slumping regime, the mean head height of the current over the smooth wall averages to $0.55h_0$. The head height is greater for uniform cubes with mean values of $0.6h_0$. The front, as it encounters the roughness peak, deflects upwards, and consequently the depth of the current increases, thus entraining more ambient fluid into the current. During the inertial regime, the

https://doi.org/10.1017/jfm.2017.678 Published online by Cambridge University Press

mean height drops to $0.5h_0$. Owing to the presence of pyramids, in both the uniform pyramids and the combination cases, irregularity in the depth of the head is evident. For the current over random cubes, a greater variation is clear, and the mean depth varies between $0.5h_0$ and $0.55h_0$ in the slumping regime; it drops to $0.48h_0$ in the inertial regime. Similar differences are observed between the current over pyramids of uniform height versus random height, where the mean h_H is $0.55h_0$ during the slumping regime, and it drops to $0.5h_0$ in the inertial regime for pyramids of uniform height, whereas the significant variation in h_H with the mean varies from $0.55h_0$ in the slumping regime to $0.45h_0$ in the inertial regime for pyramids of random height. It is clear that mean head height scales with volume fraction, as the uniform cubes with the highest volume fraction have more fluid volume in the head compared to the random pyramids with the lowest volume fraction, which have the least fluid volume in the head. Overall, the current over a rough wall entrains more ambient fluid compared to the smooth wall. Volume fraction, which is the volume occupied by the roughness elements in relation to the total volume of the channel, is an important metric that indicates roughness in the domain, and thus the greater the roughness, the higher the entrainment. The analysis has revealed that the volume fraction and solidity together dictate the differences in the flow characteristics due to surface roughness.

3.4. *Flow characteristics*

In this section, we investigate the flow structures and the modifications of the flow physics due to the presence of roughness. The time evolution of the spanwise-averaged density fields at two different times corresponding to $t = 40$ s and $t = 80$ s is shown in figure 5. At each of the times, the difference between the six cases is compared. For the smooth-wall case, the two time instants correspond to the slumping regime, and a well-defined head is one of the dominant features of the flow, which remains undiluted throughout the slumping regime (i.e. for the entire simulation). At the leading edge of the current, the nose is slightly elevated above the ground. The 2D, shear-driven, KH instabilities form at the interface of the current and the ambient fluid above it. As the current advances forwards, the distinct region of relatively undiluted head and thinning tail region are evident. At both these time instants in the slumping regime, the current has a nearly constant head height. On comparing the rough-wall cases with the smooth-wall case, a distinct head region near the leading edge of the current similar to the smooth-wall case is present. During the early stages of the slumping regime, at $t = 40$ s, the dilution of the current near the nose (leading edge) is evident, which increases with increasing roughness. At a later time, i.e. $t = 80$ s, the head region is diluted for all the roughness cases, which is distinctly different from the smooth-wall case. Similar to the smooth-wall case, the tail region is relatively undiluted for the rough-wall case. However, the depth of the tail is higher due to the presence of roughness. The increase in roughness also results in faster dilution. Owing to the presence of roughness, the nose is elevated compared to the smooth wall. For the smooth-wall case, from the studies of Samasiri & Woods (2015) and Bhaganagar (2017), the head region is relatively undiluted as the constant mixing from the ambient fluid is compensated by the high-momentum lock fluid that enters the head and maintains a nearly constant buoyancy till the end of the slumping phase. However, surface roughness causes higher wall shear, resulting in a slowing down of the high-speed lock fluid, and hence resulting in faster dilution and mixing during

https://doi.org/10.1017/jfm.2017.678 Published online by Cambridge University Press

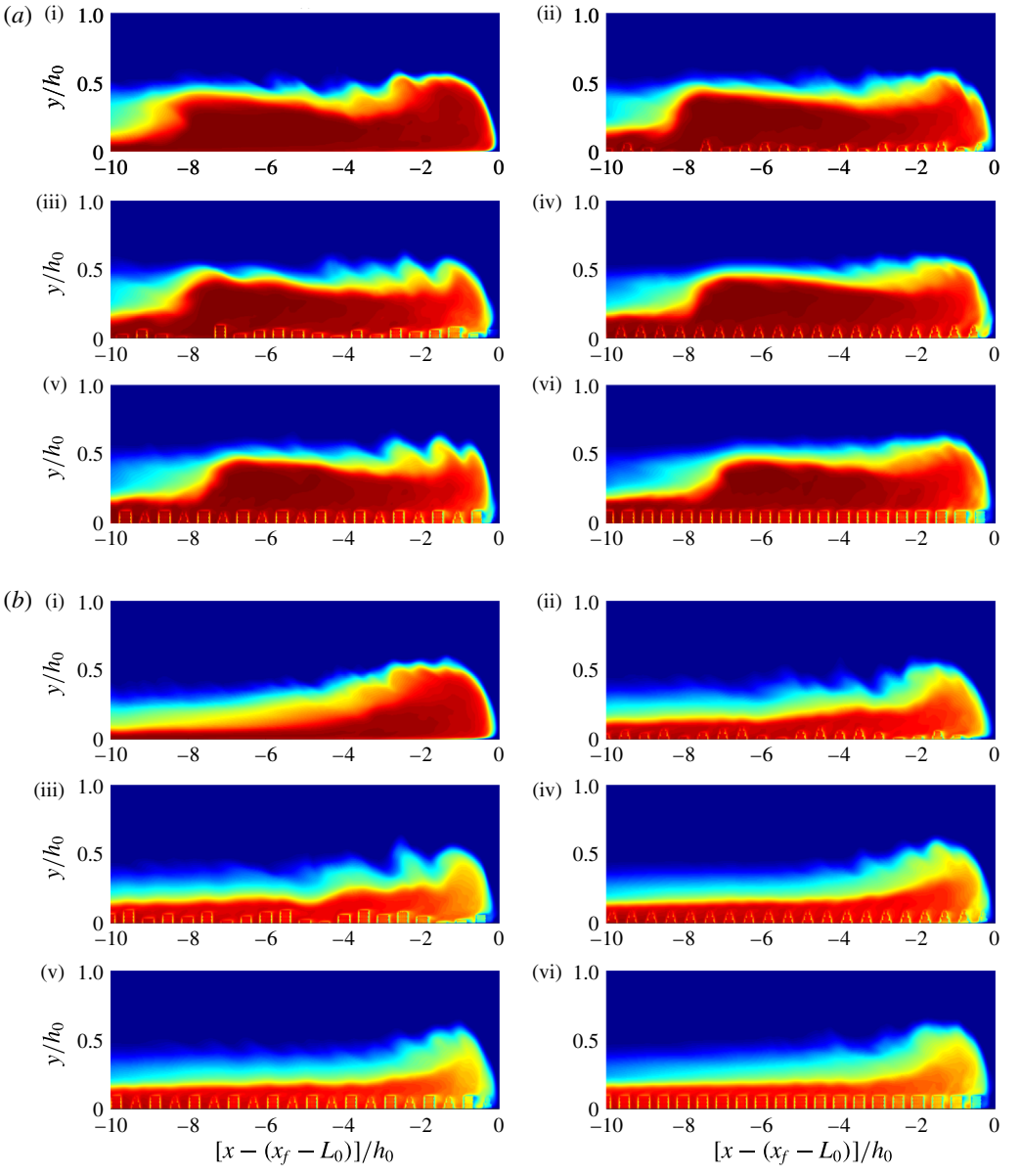


FIGURE 5. (Colour online) Evolution of the spanwise-averaged density field in a frame-invariant distribution with origin placed at the nose: (*a*) time = 40 s, (*b*) time = 80 s. The roman numerals represent (i) smooth bed (SB), (ii) pyramids with random height (PR), (iii) cubes with random height (CR), (iv) pyramids with uniform height (PU), (v) cubes and pyramids with uniform height (CPU), and (vi) cubes with uniform height (CU). Blue color represents density of the ambient fluid and red represents the undiluted lock fluid. The intermittent color distributions identify the dilution occuring on account of mixing.

the slumping regime. Overall, it is clear that, with identical initial conditions and for the same elapsed time, the head region is much diluted for rough cases compared to the smooth wall. The density fields clearly indicate increased mixing in the head

https://doi.org/10.1017/jfm.2017.678 Published online by Cambridge University Press

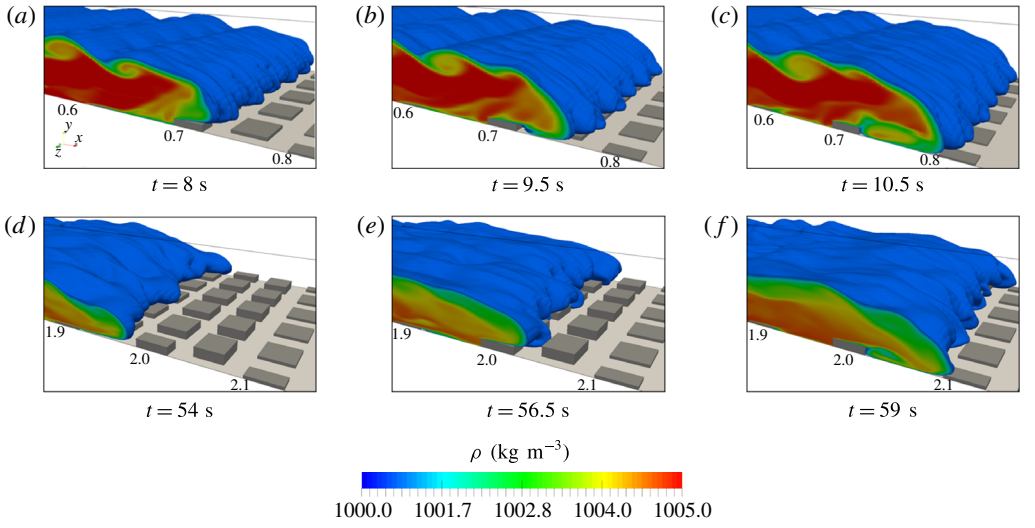


FIGURE 6. (Colour online) For the roughness comprising cubes of random elevations (CR), the iso-volumes of the density field (plotted up to 10 % threshold) are illustrated at selected time steps.

region with increasing roughness, and more mixing occurs near the front end of the current.

3.4.1. *Flow structures*

To understand the effect of roughness in altering the flow characteristics of the current, we now focus on the one case of random cubes. Figure 6(*a–c*) and (*d–f*) show the front advancing over cubes of random elevations in accelerating and slumping phases, respectively. The 2D KH instabilities develop early on during the acceleration regime and lead to the formation of the 3D characteristic lobe–cleft instabilities. As the front evolves, the lobe–cleft instabilities have a distinct signature of the underlying roughness elements. Furthermore, during the accelerating regime, the head region of the current forms, and the shape of the head also has a signature of the underlying roughness features. During this regime, the current is nearly filled with heavy fluid. There are 78 rows of roughness elements in the domain, between $7.2h_0 \leqslant x_f \leqslant 8h_0$; the front is crossing over the 14th row of roughness. In this row, the roughness elements have a height of up to $0.067h_0$, as the front approaches them; because of the abrupt change in flow direction, portions of the head jump vertically up to the height of $0.4h_0$ and subsequently attach to the upper roughness surface. Owing to this impact, the front loses its momentum locally, yet convects over cubical obstructions by virtue of its potential energy. Crossing over the obstruction, the front splashes down towards the bottom bed at a distance of $d \approx RH_n$ (subscript n denotes the nth row of roughness elements whose height is RH) downstream. Pockets of ambient fluid get trapped in the current in the valley region. Similar observations have been made by Tokyay *et al.* (2011). The trapped ambient fluid gains momentum and the shear results in an additional local circulation, thus pushing these pockets into the heavy fluid propagating above them (figure 6*c*). The heavy fluid flowing between roughness features acts as a catalyst in this mixing. However, this behaviour is localized, and exhibits strong coupling to the availability and height of roughness features, and

https://doi.org/10.1017/jfm.2017.678 Published online by Cambridge University Press

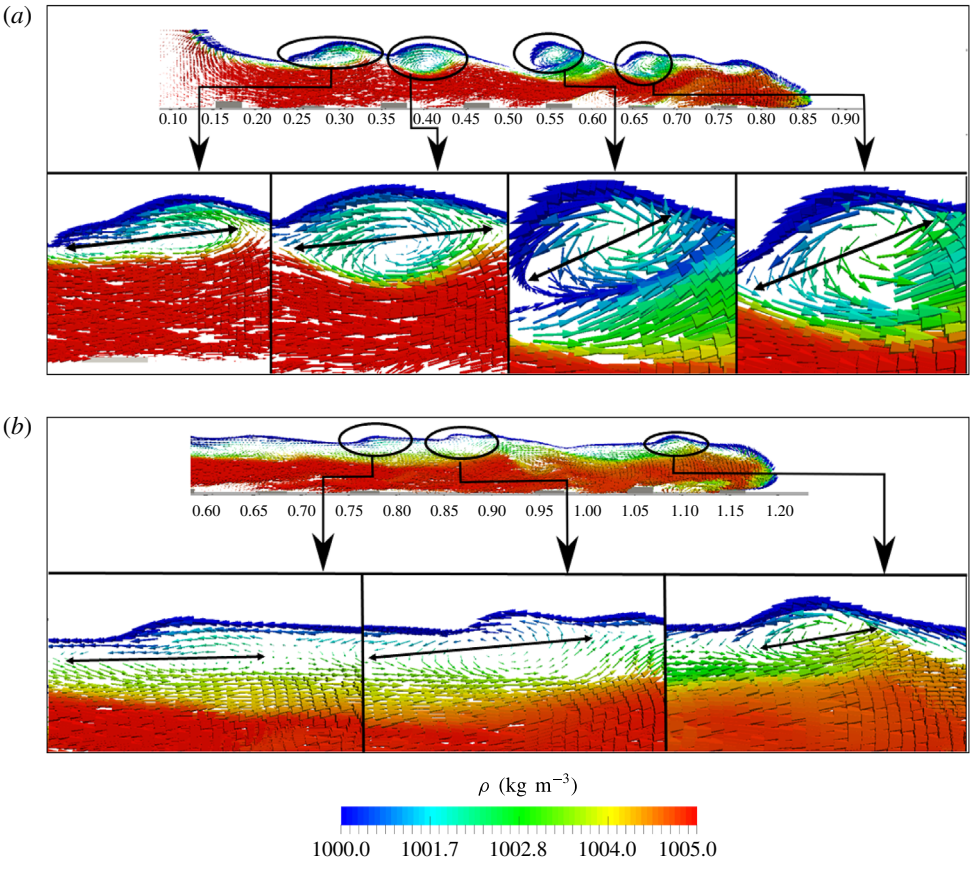


FIGURE 7. (Colour online) Front view of velocity fields during the (*a*) acceleration and (*b*) slumping phases for the current advancing over cubes of random height (CR). The colour distribution is in accordance with the density distribution whereas the arrows mark the direction of the velocity vector field. The horizontal scale signifies the dimensional distance in metres from the back (slip) wall of the channel.

the potential energy of the head. Furthermore, the impact between the front and the roughness features generates turbulent eddies, which in turn accelerate mixing in the head.

Substantial mixing also takes place via KH rollers at the shear interface, as seen in figure 7(*a*,*b*), illustrated by the velocity vectors plotted on a plane positioned midspan, during the two instants of the slumping regime. The colour distribution is set proportional to the density concentration to convey the idea of ambient fluid entering the current. Here, KH rollers can be seen creating a strong circulation, resulting in the ambient fluid being entrained into the current. During the initial phases (figure 7*a*), distinct regions of circulation are located at $x = 2.5h_0$, $4h_0$, $5.6h_0$ and $6.75h_0$. As the current advances and within the slumping regime, the presence of additional shear stretches the circular mixing zones into elliptical recirculating zones. In figure 7(*b*), these recirculating regions are at $x = 7.4h_0$, $8.4h_0$ and $11h_0$. Furthermore, as seen in figure 8, there is a recirculating region formed near the leading edge of the current that displaces the ambient fluid, and a fraction of the

https://doi.org/10.1017/jfm.2017.678 Published online by Cambridge University Press

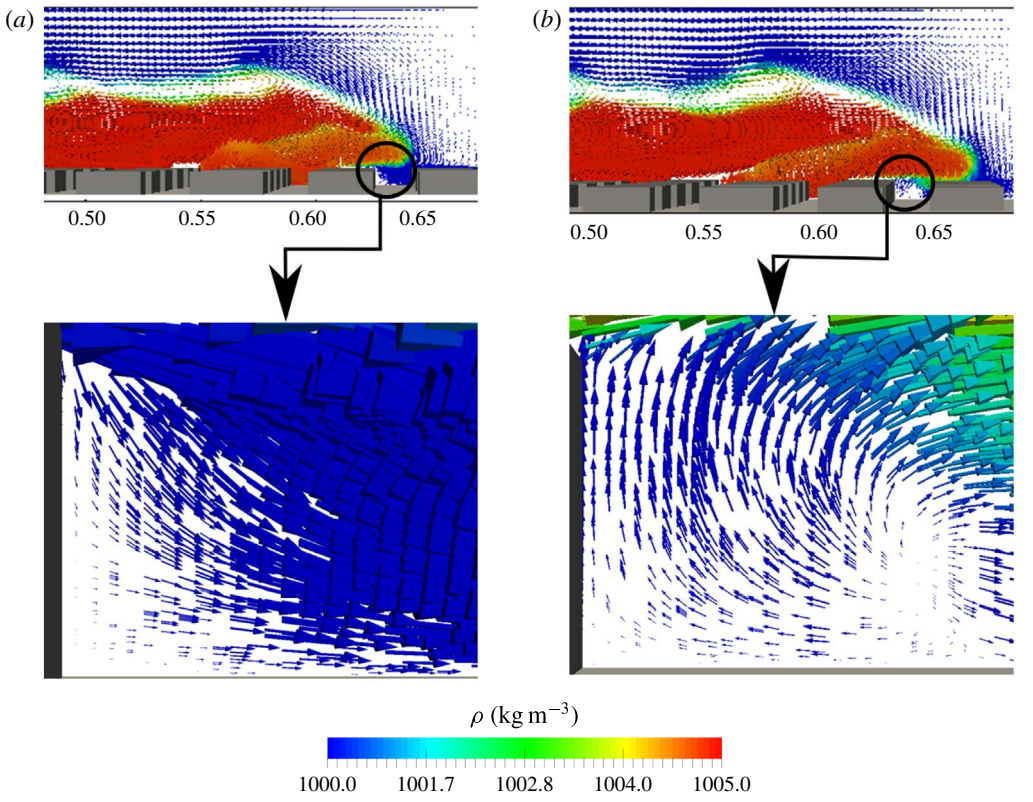


FIGURE 8. (Colour online) Nose is crossing over a row of bottom roughnesses comprising cubes of uniform elevation (CU). Panels (*a*) and (*b*) are captured on a 2D plane at $t = 4.5$ s and 5.5 s, respectively. The colour distribution is in accordance with the density whereas the arrows mark the direction of the velocity vectors. The illustration clearly depicts circulation in the wake of a roughness feature and the consequent dilution. The horizontal scale signifies the dimensional distance in metres from the back (slip) wall of the channel.

ambient fluid enters the current and the remainder is pushed in the opposite direction from the front. These findings are consistent with those of Kneller *et al.* (1999), who used laser Doppler anemometry to reveal, for a smooth wall, a vortex near the head with strong circulation within the head region. In addition to the mixing that happens at the current interface, it is clearly seen in figure 8 that, as the current travels between the two successive roughness elements, the ambient fluid trapped between the roughness elements gains momentum, and the shear results in a local recirculation region between the roughness elements. The additional vorticity that is generated causes the ambient fluid to mix with the mixed fluid, further diluting the current. This additional dilution is local and occurs between the roughness elements. This can be further understood by examining the top view in figure 9. It shows the velocity vectors plotted on a plane lying halfway between the roughness height for the domain containing cubes of uniform height. The vectors are coloured according to density distribution. As the current passes over the roughness elements, the portion over the roughness peaks slows down, and that flowing between the valley regions accelerates. At $t = 50$ s, the heavy fluid traverses over the roughness peaks, resulting

https://doi.org/10.1017/jfm.2017.678 Published online by Cambridge University Press

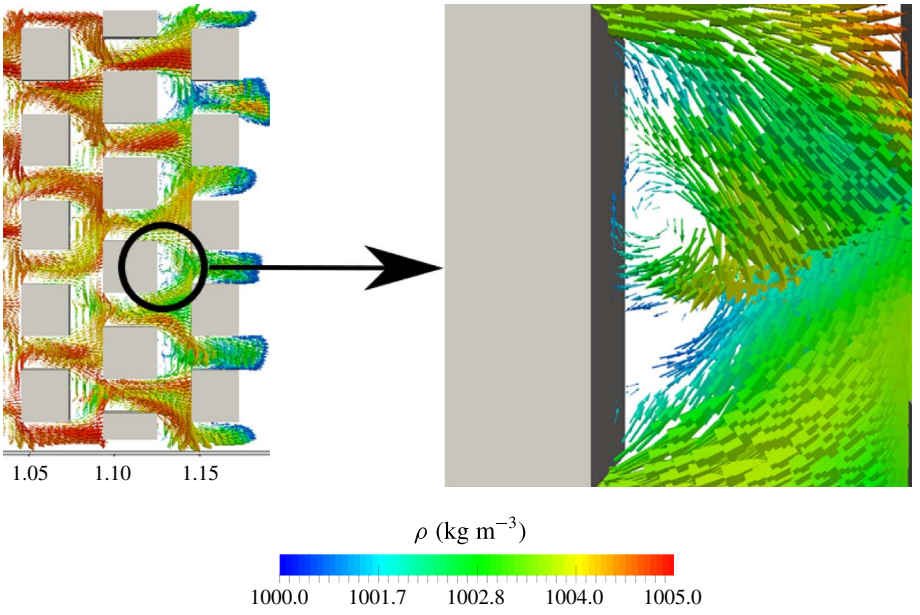


FIGURE 9. (Colour online) Flow field plotted on a plane normal to the elevation as the nose crosses a row of bottom roughnesses comprising cubes of uniform elevation (CU). The arrows mark the direction of the velocity vectors whereas the colour distribution is in accordance with the local density distribution. The horizontal scale signifies the dimensional distance in metres from the back (slip) wall of the channel.

in the formation of a shear layer that disturbs the ambient fluid in the valley regions of the roughness, which mixes with the current and the mixed fluid that passes through the valleys.

The additional mixing occurs due to roughness elements that act as mixing rollers that mix the trapped ambient fluid under the frontal region of the current with the mixed fluid within the current, resulting in additional dilution. Now the question that needs to be investigated is this: What metric dictates the amount of mixing and dilution that takes place due to the presence of roughness? Roughness elements are more efficient generators of skin friction than their smooth counterparts, and hence the rough wall has greater shear, and consequently greater Re_τ compared to a smooth wall (e.g. Bhaganagar *et al.* 2004; Jimenez 2004; Orlandi & Leonardi 2004). The shear layer developed in the roughness region is analysed next.

3.5. *Shear stress*

Figure 10 shows the spanwise-averaged shear plotted in the x–y plane for all the cases compared at $t \approx 67.5$ s. Regions of high shear are seen at the interface near the head, and near the lower wall. The KH rollers cause the large velocity gradients at the interface in the head region. Additionally, high wall shear stress is in region $x = 20$–25, and this corresponds to $x/L_0 = 1$, which is one lock length. At the lower wall, due to the no-slip condition, the shear layer emanates from the wall. Bhaganagar (2017) observed that entrainment occurs within one lock length from the nose, and that the region is designated as the active head region of the current. For all the rough cases (figure 10*b–f*), similar to the smooth wall, high shear at the interface is mainly in

https://doi.org/10.1017/jfm.2017.678 Published online by Cambridge University Press

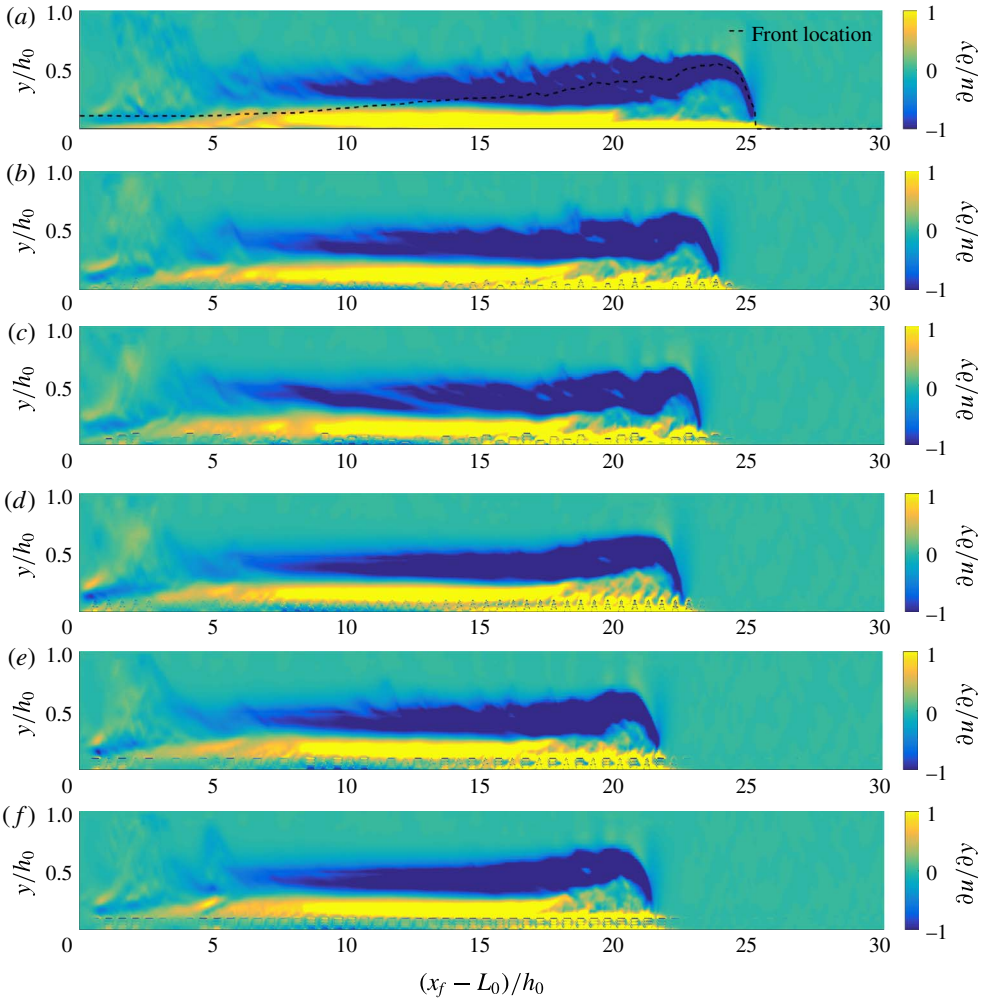


FIGURE 10. (Colour online) Contours of shear distribution calculated from the spanwise-averaged streamwise velocity field plotted at $t = 67.5$ s: (*a*) smooth bed (SB), (*b*) pyramids with random height (PR), (*c*) cubes with random height (CR), (*d*) pyramids with uniform height (PU), (*e*) cubes and pyramids with uniform height (CPU), and (*f*) cubes with uniform height (CU).

the head region of the current, and this is due to the KH rollers. In addition, large wall shear exists on roughness peaks, and thus exhibits a signature of roughness. An important difference that exists between the smooth wall and the rough wall is the following. For the smooth wall, strong shear layers exist at the interface of the current and ambient fluid as well as in the neighbourhood of the bottom wall. The latter is a thin layer, and no interaction takes place between the two shear layers. In the case of the rough wall, a similar shear layer at the interface of the current and ambient fluid exists; however, the shear layer at the rough (bottom) wall is stronger and deeper, and has a signature of the underlying roughness. To get clarity on the strength of the shear layer at the interface versus the lower rough wall, we plot maximum shear at the interface versus front location in figure 11(*b*), and the friction Reynolds number,

https://doi.org/10.1017/jfm.2017.678 Published online by Cambridge University Press

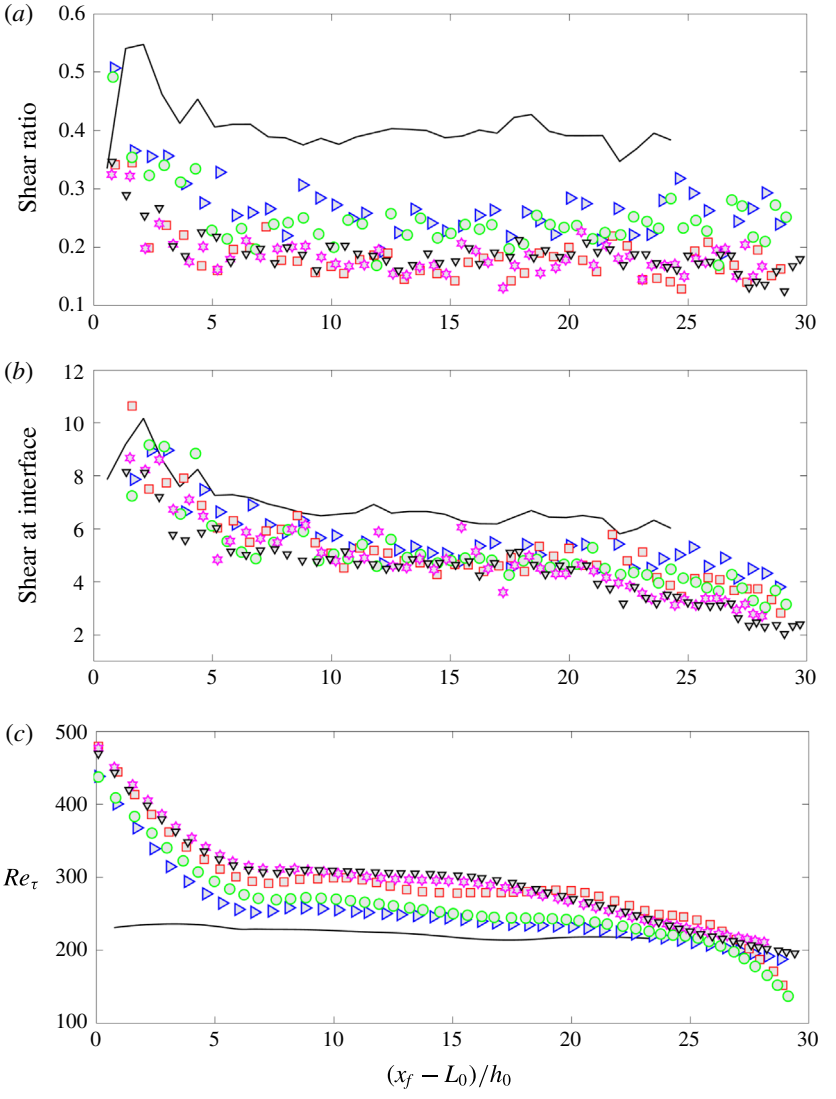


FIGURE 11. (Colour online) (*a*) Ratio of the shear at the interface to the shear at the rough wall versus front location. (*b*) Maximum shear recorded at the interface. (*c*) Friction Reynolds number. See figure 3 for key.

Re_τ, obtained from wall shear stress, versus front location in figure 11(*c*), respectively. The rough wall has a higher Re_τ compared to the smooth wall, as expected, and differences between the roughness geometries exist. The values of Re_τ range between 245 and 306 (in the slumping phase). However, the maximum values occur right after the lock release, and the value is as high as 500. As the current advances forwards, wall shear is nearly constant with Re_τ of 220 throughout the slumping regime for the smooth-wall case. During the slumping regime, the uniform cubes have the highest Re_τ of 306, followed by cubes and pyramids of uniform height with Re_τ of 298, cubes of random height with Re_τ of 285, pyramids of uniform height with Re_τ of 258, and finally, pyramids of random heights with Re_τ of 245. Therefore, Re_τ is a

https://doi.org/10.1017/jfm.2017.678 Published online by Cambridge University Press

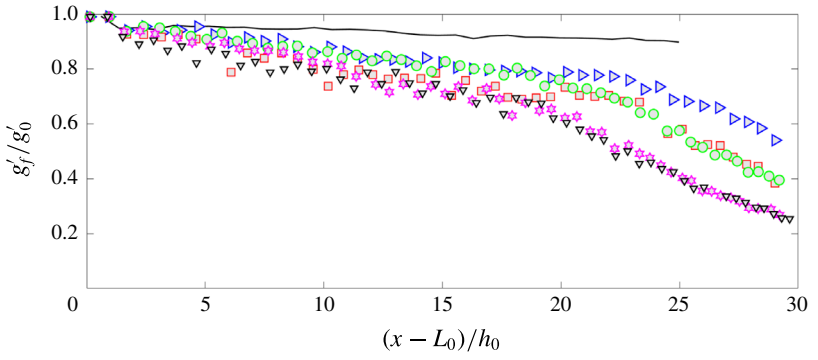


FIGURE 12. (Colour online) Local reduced gravity g_f' scaled with the initial reduced gravity g_0' in the lock versus the front location. See figure 3 for key.

representation of the dynamics of roughness, and in the subsequent analysis, presented in the next section, it is demonstrated that Re_τ is the key metric that represents the influence of roughness on enhanced mixing in the current. Finally, to get clarity on the relative magnitude of the shear layer at the interface versus the lower wall, the ratio of maximum shear at the interface to that of the bottom bed is plotted in figure 11(*a*). After the initial transience, the maximum shear at the interface of the current and ambient fluid is around 0.4, whereas for the rough wall this shear is lower (in the range of 0.15–0.3, depending on the roughness). The fraction of the shear due to KH rollers, with respect to wall shear, is smaller for the rough wall compared to the smooth wall. Scaled by the wall roughness, the KH rollers are weaker due to the presence of roughness.

3.6. *Mixing and entrainment*

Next, we quantify the mixing process based on the reduced gravity at the front (g_f'), defined as $g_f' = \widetilde{g_e'}\widetilde{h}_H/h_H$, where $\widetilde{g_e'}\widetilde{h}_H = g\int_0^{h_0}[(\rho(x^*, y, t) - \rho_L)/\rho_L]\,\mathrm{d}y$. In figure 12, g_f' scaled by the initial reduced gravity (g_0'), defined as $g_0' = g(\rho_H - \rho_L/\rho_L)$, is plotted as a function of x_f. For the smooth wall, the current is entirely in the slumping regime, and g_f is nearly constant at a fraction of 0.9–1.0 of the original lock fluid, which implies that the local buoyancy in the head does not change when the current is in the slumping regime. In the roughness cases, a notable difference is that more mixing is evident. Two regimes are clearly evident from figure 12 for the rough-wall cases. Unlike the smooth wall, the rough wall shows more variation within the slumping regime, as g_f' varies between 0.8 and 0.9, which indicates that mixing due to roughness starts early on in the slumping regime, causing dilution and thus reduction in buoyancy. A consistent trend is observed in the front trajectory, as seen in figure 3(*a*), where, during the slumping regime, there is a loss of buoyancy and the slope of the front trajectory varies between 0.92 and 0.99. In the next regime, high dilution and mixing is evident for the rough-wall case. In addition, significant differences between the rough-wall cases are evident in the inertial regime. The greater the roughness, the faster is the dilution at the front. In the inertial regime, for uniform cubes, g_f' drops from 0.8 to 0.1 by the time the front reaches $x = 30h_0$ from the gate. A similar trend is also evident for the combination of cubes and pyramids of uniform height. For the same distance, the dilution for random pyramids is from

https://doi.org/10.1017/jfm.2017.678 Published online by Cambridge University Press

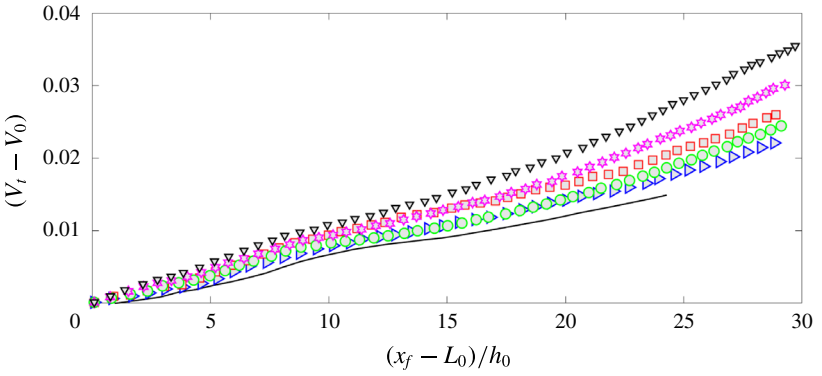


FIGURE 13. (Colour online) Change in volume of the current with respect to the initial lock volume plotted against the front location. See figure 3 for key.

0.9 to 0.5. In the other cases the dilutions are between these values, from 0.8 to 0.3 for random cubes, and from 0.9 to 0.4 for random pyramids. As a note, an alternative definition of bulk reduced gravity in the head has been used to evaluate the reduced gravity and no significant difference has been observed in the mixing, in either the slumping or inertial regimes, thus giving us confidence that the front is a representation of mixing in the head for rough walls as well.

The instantaneous entrainment parameter is the amount of ambient fluid that enters the current, and hence is defined as the increase in the volume of the fluid in the current from the initial lock volume in time t scaled by the length of the current (distance between the nose and the tail or lock gate) and the velocity of the front (u_f):

$$E_l(t) = \frac{V(t) - V_0}{l u_f t}. \tag{3.1}$$

Here, $V(t)$ is the volume of the dense fluid, V_0 is the volume of the initial lock fluid and l is the length of the current. The volume of the current is defined as $V(t) = \int_0^{x_f} h(x, t)\,\mathrm{d}x$. Figure 13 shows $V(t)$ versus nose location (x_f). For the smooth wall, after an initial acceleration period, the volume increases at a non-uniform rate. The volume occupied under the current is higher for rough walls, and this increases with increasing roughness. The greater the volume fraction of roughness, the greater the volume occupied by the mixed fluid in the current.

Figure 14 shows instantaneous entrainment coefficient E on the primary y-axis versus the front location for all the cases. The vertical lines represent the location where the front transitions from the slumping to the inertial regime. In figure 14, Re_τ is plotted on the secondary y-axis. Also shown is the slope of E versus x_f, which has been calculated separately in the slumping and inertial regimes. As the volume fraction increases, the slope of E versus x_f increases from 1.45×10^{-4} to 6.03×10^{-4}. By the end of the slumping regime, E reaches a quasi-equilibrium value, as seen from the slope in the inertial regime, which is at least one order of magnitude less than that in the slumping regime. The observation for the rough-wall cases is that, with increasing volume fraction, entrainment during the beginning of the slumping regime is higher, the rate at which the entrainment drops (slope) is faster, and the final steady-state value reached at the end of the slumping regime is higher. As seen from Re_τ (secondary y-axis) versus x_f in figure 14, during the slumping regime Re_τ

https://doi.org/10.1017/jfm.2017.678 Published online by Cambridge University Press

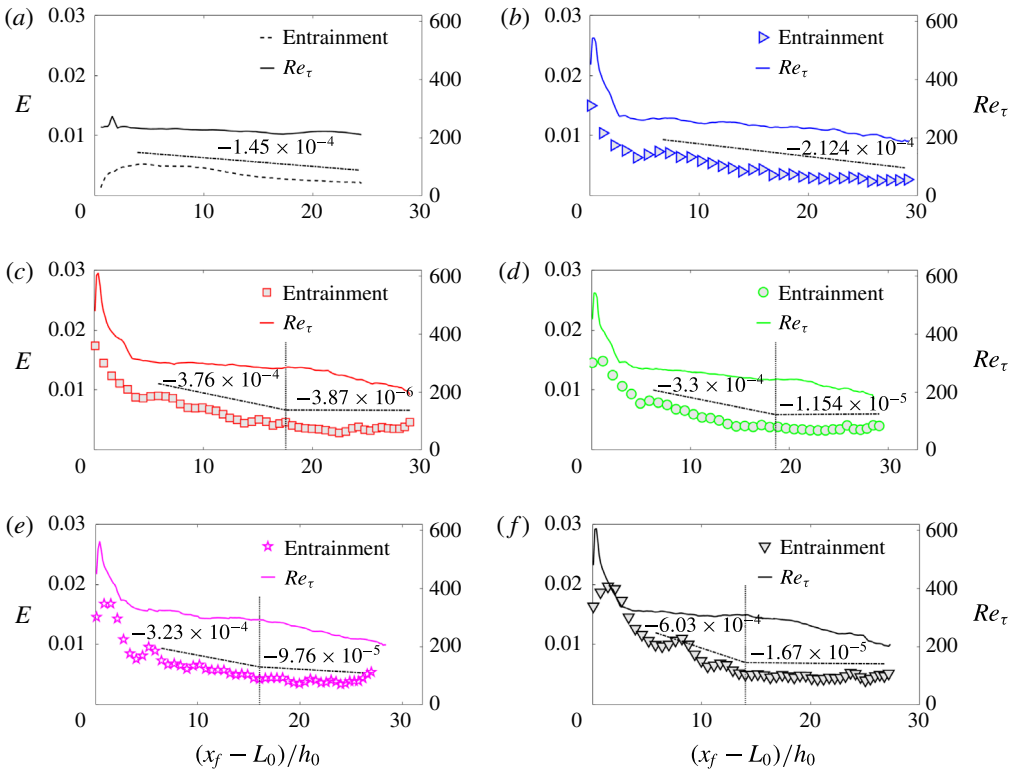


FIGURE 14. (Colour online) Variation in entrainment coefficient and turbulent Reynolds number: (*a*) smooth bed (SB), (*b*) pyramids with random height (PR), (*c*) cubes with random height (CR), (*d*) pyramids with uniform height (PU), (*e*) cubes and pyramids with uniform height (CPU) and (*f*) cubes with uniform height (CU).

Case	Shape	Elevation	Re	Fr	Re_τ	E	Shear ratio
1 (SB)	Smooth bed	—	1591.07	0.561	223.048	0.00257	0.407
2 (PR)	Pyramids	Random	1420.98	0.521	245.485	0.00296	0.252
3 (CR)	Cubes	Random	1348.92	0.486	286.665	0.00382	0.186
4 (PU)	Pyramids	Uniform	1293.69	0.461	255.401	0.00365	0.236
5 (CPU)	Cubes + Pyramids	Uniform	1289.25	0.4436	300.774	0.00398	0.176
6 (CU)	Cubes	Uniform	1371.11	0.422	305.630	0.00473	0.174

TABLE 2. Averaged values of Re, Fr, Re_τ, E and shear ratio during the slumping regime.

does not show significant variation, and it drops drastically during the inertial regime, as the drag due to roughness dominates the flow dynamics. The higher the volume fraction, the higher is the E value during the slumping regime. This trend is clearly seen in table 2, where the averaged values of E, Re, Fr and Re_τ during the slumping regime are presented. A strong correlation exists between E and Re_τ.

Though the focus of this study is to shed light on the unsteady nature of mixing in the density current, we calculate the mean values of E averaged over the slumping regime and present them in figure 15(*a*,*b*). Here, the mean E is plotted against the

https://doi.org/10.1017/jfm.2017.678 Published online by Cambridge University Press

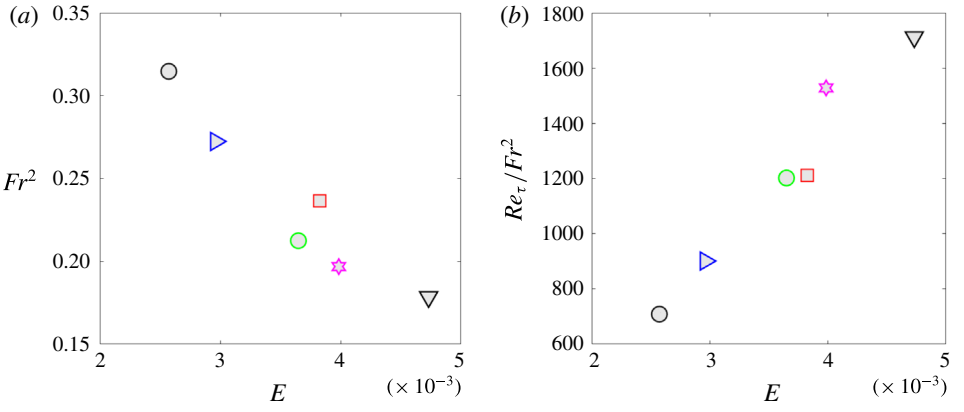


FIGURE 15. (Colour online) Mean entrainment coefficient in the slumping phase plotted against (*a*) the square of the mean Froude number (Fr^2) and (*b*) the ratio of Re_τ and Fr^2. See figure 3 for key.

averaged value of (Fr^2) and Re_τ/Fr^2, respectively. The average Fr^2 correlates with E for some cases, but discrepancy in the correlation is seen. We have observed that Fr correlated with the spanwise solidity, and that E correlated with volume fraction; hence, the trend observed is expected, and Fr is lower for random pyramids than for random cubes, but the entrainment coefficient for random cubes is higher than for random pyramids. A better correlation of E with Re_τ/Fr^2 is seen in figure 15(*b*). It should be noted that the average Re for all the roughness cases considered varies within a smaller range of 1290–1420 (see table 2). To understand the effect of Re on this relation with E, additional experiments, e.g. with different initial conditions, are needed. It is clear that for the low-Reynolds-number density currents with roughness elements within the current, in addition to Fr, the entrainment coefficient also depends on Re_τ.

4. Conclusions

LES have been conducted to simulate 3D lock-exchange release density currents over smooth and rough surfaces. A highly accurate and novel penalization-based method has been developed to introduce complex geometry. The primary objective of this work is to establish a firm foundation for the effect of surface roughness on front characteristics and mixing in the current. Surface roughness adds significant complexity both to the flow dynamics and to the flow analysis. Study of rough walls is complicated due to the influence of various roughness parameters that the wall introduces into the flow physics. The distribution and shape of roughness elements are important indicators that influence the flow dynamics; hence the differences that exist between roughness elements with the same height versus those with irregular heights are important.

The near-wall region of the density current has a significant role in modifying the flow dynamics, and wall shear (τ_w) dictates the drag encountered by the current. Among the roughness metrics, the roughness density is the metric that influences τ_w. In this study, the volume fraction and roughness solidity were varied by changing the shapes of cubes and pyramids (stepped cubes) with uniform height and random height distributions. The simulations were performed under the same conditions, including

https://doi.org/10.1017/jfm.2017.678 Published online by Cambridge University Press

domain size, lock conditions (height and aspect ratios) and with the same initial reduced gravity and buoyancy.

Surface roughness has an important effect on density currents, and it significantly alters the front characteristics and mixing within the current. The potential-energy method developed by Anjum *et al.* (2013) provides a consistent approach to obtain the current depth, as it is unambiguous, unlike the commonly used threshold method. We develop a consistent manner to estimate the interface height, front height (height of the head) and definitions of *Fr* and *Re*, which is suitable for rough surfaces. It is important for future studies on roughness to use consistent and accurate definitions that define the front. As per Benjamin's (1968) theory, the curvature of the current switches from being negative to being positive near the nose, and hence the inflection point of the maximum density at each streamwise location x defines the nose (x_f) and the rate of the change of x_f is the front velocity (u_f).

Peters & Venart (2000) conducted experiments on density currents over 2D square cross-sectional elements and obtained constant slopes of 0.91 ± 0.04 during the slumping regime, and $2/3$ in the inertial regime. It is important to note that the slumping regime does exist for the rough wall, where the current moves with nearly uniform velocity, but the slope of the front trajectory is not exactly unity, as in the smooth-wall case. The main difference is that the buoyancy is conserved during the slumping regime, whereas a low amount of mixing is present for rough-wall cases, as the shear layer near the roughness elements acts as an efficient mixing roller during the early stages of the slumping regime. For all the roughness cases considered, two distinct regimes are clearly evident. During the slumping regime, the mixing as obtained from the reduced gravity is between 0.8 and 1.0, indicating some loss of buoyancy in the slumping regime. This is followed by an inertial regime, with faster loss of buoyancy as the front advances.

Surface roughness slows down the density currents and *Fr* decreases with increasing streamwise solidity (Γ_1), as the front velocity depends on the ratio of roughness area blockage with respect to the cross-sectional area facing the front. A well-defined head is evident for currents over roughness in the slumping regime, and the shape of the head has a signature of the underlying roughness features. As the current travels between two successive roughness elements, the ambient fluid trapped between the roughness elements gains momentum, and the shear results in a local recirculation region between the roughness elements. The additional vorticity that is generated causes the ambient fluid to mix with the mixed fluid, further diluting the current. This additional dilution is local and occurs between the roughness elements. Increased surface roughness over which the density current flows leads to increased wall shear stress, mainly in the head region of the current. Density currents over roughness surfaces have higher deceleration and increased mixing.

Flow visualization has revealed that, during the early stages of slumping, the KH rollers are circular, but the shearing acting on the interface elongates these rollers during the later stages of slumping. This is different than for smooth walls (figures are not shown for smooth walls). The elongation causes the strength of KH rollers to weaken. The strength of the KH rollers has been evaluated from the shear at the interface (figure 11*b*). The KH rollers are weaker for a rough wall compared to a smooth wall. It is interesting to note that the differences due to the near-wall influence of roughness does not influence the strength of KH instability, and hence the mean shear at the interface (averaged during the slumping regime) is nearly the same for all the roughness cases, suggesting that roughness reduces the strength of KH rollers compared to the smooth-wall case; however, the differences in roughness

https://doi.org/10.1017/jfm.2017.678 Published online by Cambridge University Press

shape and distribution do not influence them significantly. It is very likely that the strength of the KH rollers is influenced by the initial conditions of the lock. The velocity vectors indicate that, as the current moves over the roughness peaks, the shear layer generated from the peaks is strong, and depends on the roughness, and it is comparable in strength to the KH shear layer. The behaviour is similar to that observed in constant-density flows over roughness, where the roughness causes the shear layer lift-up. The ambient and stationary fluid in the valleys gains momentum and the shear layer formed over the roughness propels the fluid vertically upwards, thus generating vorticity in this region, the consequence of which is additional mixing and dilution of the current. In principle, the entrainment occurs from two sources: the primary source of entrainment is at the interface, where the shear entrains the ambient fluid near the interface, which has been displaced by the current; and the secondary source is due to the shear layer lift-up (as seen in figure 10) resulting in roughness-induced vorticity that causes additional mixing. For the primary source of entrainment, the extent of mixing is mainly dictated by front conditions (namely, Re). For the latter, the roughness-induced vorticity is mainly dictated by the amount of wall shear generated by the roughness. Hence, a measure of the wall shear stress dictates the latter source of entrainment.

The instantaneous entrainment coefficient, defined as the increase in the volume of the fluid in the current from the initial lock volume in time t scaled by the length of the current (distance between the nose and the tail or lock gate) and the velocity of the front, revealed insightful information on the unsteady entrainment process. For the rough-wall cases with increasing volume fraction we have the following results: entrainment during the beginning of the slumping regime is higher; the rate at which the entrainment drops (slope of E and x_f) is faster; and the final steady-state value reached at the end of the slumping regime is higher. It is clear that entrainment begins during the early stages of the slumping regime, and the rate of entrainment is at least an order of magnitude higher during the slumping regime than in the inertial regime. Finally, as shown in table 2, where the averaged E has been calculated during the slumping regime, it shows a trend with the averaged Re_τ. It should be noted that, for the roughness cases selected in the study, Re varies within a smaller range of 1290–1420.

The high-resolution LES simulations of Tokyay *et al.* (2012) for 2D dunes and 2D ribs demonstrated that the spatial distribution of the friction velocity u_τ can be correlated to entrainment. In this study, we demonstrate that Re_τ based on u_τ and the local height of the current (h_H) is an appropriate metric that quantifies the additional entrainment and mixing that results due to the roughness dynamics. The study provides further support to the theory posed by Fernandez & Imberger (2006) that entrainment depends on the stress generated at the bottom, and obtained by the roughness and the current properties. The present study is novel and presents a framework for analysing entrainment of density currents over roughness. It is important to conduct future experimental and numerical studies for a much larger range of roughness volume fraction and solidity under different Re conditions. This study is one of the first to conduct an analysis of the unsteady nature of the entrainment during the slumping and inertial regime over 3D roughness, and it clearly demonstrates an important need to study the entrainment process in time. These future studies will provide guidance to relate local entrainment to current properties (namely, Re and Fr) and roughness properties (Re_τ).

https://doi.org/10.1017/jfm.2017.678 Published online by Cambridge University Press

Acknowledgements

Funding for this research was provided by the National Science Foundation, Division of Physical Oceanography grant no. OCE-1333033, and US Army Edgewood Chemical and Biological Center, MSRDC grant no. D01-W911SR-14-2-0001-0006. The authors acknowledge the Texas Advanced Computing Center (TACC) at the University of Texas at Austin (http://www.tacc.utexas.edu) for providing computational and visualization resources that have contributed to the research results reported within this paper.

Appendix A. Symbols and notation

$g_0' = g(\rho_H - \rho_L)/\rho_L$	initial reduced gravity
$g_f' = g(\rho_{x^*} - \rho_L)/(\rho_H - \rho_L)$	local reduced gravity
ρ_{x^*}	density field at the streamwise location x^*; see (2.15) for the definition of x^*
$\rho^* = (\rho_{xy} - \rho_L)/(\rho_H - \rho_L)$	non-dimensional density at 2D spatial location x, y
ρ_{th}	threshold density
$\rho_m = \max_z[\rho^*(x, z, t)]$	maximum non-dimensional density at each streamwise location
$\tau_w - \max[(\partial u_x/\partial y)\big\|_{x,y=0}^{x,y=h_0}]$	wall shear
$g_f' = \int_0^{h_0} \rho(x^*, t)\,\mathrm{d}h$	
$Re = (u_f h_H)/\nu$	
$Fr = u_f/\sqrt{g_0' h_H}$	
$u_\tau = \sqrt{\nu(\partial u_x/\partial y)\big\|_{x,y=0}^{x,y=h_0}}$	friction velocity
$Re_\tau\|_x = [(\max_y(u_\tau))_x h_H]/\nu$	

REFERENCES

ADDUCE, C., LOMBARDI, V., SCIORTINO, G. & MORGANTI, M. 2009 Roughness effects on gravity currents dynamics. In *Proceedings of the 33rd IAHR Congress, Canada*. International Association for Hydro-Environment Engineering and Research.

ANGOT, P., BRUNEAU, C.-H. & FABRIE, P. 1999 A penalization method to take into account obstacles in incompressible viscous flows. *Numer. Math.* **81** (4), 497–520.

ANJUM, H. J., MCELWAINE, J. N. & CAULFIELD, C.-C. P. 2013 The instantaneous Froude number and depth of unsteady gravity currents. *J. Hydraul. Res.* **51** (4), 432–445.

BARR, D. I. H. 1963 Densimetric exchange flow in rectangular channels. I. Definitions, review and relevance to model design. *La Houille Blanche* **1** (7), 739–756.

BENJAMIN, T. B. 1968 Gravity currents and related phenomena. *J. Fluid Mech.* **31** (02), 209–248.

BHAGANAGAR, K. 2014 Direct numerical simulation of lock-exchange density currents rough wall in slumping regime. *J. Hydraul. Res.* **52** (3), 386–393.

BHAGANAGAR, K. 2017 Role of head of turbulent 3-D density currents in mixing during slumping regime. *Phys. Fluids* **29** (2), 020703.

BHAGANAGAR, K. & CHAU, L. 2015 Characterizing turbulent flow over 3-D idealized and irregular rough surfaces at low Reynolds number. *Appl. Math. Model.* **39** (22), 6751–6766.

BHAGANAGAR, K., KIM, J. & COLEMAN, G. 2004 Effect of roughness on wall-bounded turbulence. *Flow Turbul. Combust.* **72** (2), 463–492.

BORDEN, Z. & MEIBURG, E. 2013 Circulation based models for Boussinesq gravity currents. *Phys. Fluids* **25** (10), 101301.

https://doi.org/10.1017/jfm.2017.678 Published online by Cambridge University Press

BRINKMAN, H. C. 1949 On the permeability of media consisting of closely packed porous particles. *Flow Turbul. Combust.* **1** (1), 81.

BRITTER, R. E. & SIMPSON, J. E. 1978 Experiments on the dynamics of a gravity current head. *J. Fluid Mech.* **88** (02), 223–240.

CANTERO, M. I., BALACHANDAR, S., GARCÍA, M. H. & FERRY, J. P. 2006 Direct numerical simulations of planar and cylindrical density currents. *Trans. ASME J. Appl. Mech.* **73** (6), 923–930.

CENEDESE, C., NOKES, R. & HYATT, J. 2017 Lock-exchange gravity currents over rough bottoms. *Environ. Fluid Mech.*, doi:10.1007/s10652-016-9501-0.

CHAU, L. & BHAGANAGAR, K. 2012 Understanding turbulent flow over ripple-shaped random roughness in a channel. *Phys. Fluids* **24** (11), 115102.

COUNEHAN, J. 1971 Wind tunnel determination of the roughness length as a function of the fetch and the roughness density of three-dimensional roughness elements. *Atmos. Environ.* **5** (8), 637–642.

DE MARCHIS, M. & NAPOLI, E. 2012 Effects of irregular two-dimensional and three-dimensional surface roughness in turbulent channel flows. *Intl J. Heat Fluid Flow* **36**, 7–17.

ERGUN, S. 1952 Fluid flow through packed columns. *Chem. Engng Prog.* **48**, 89–94.

FANNELOP, T. K. & WALDMAN, G. D. 1971 The dynamics of oil slicks – or 'creeping crude'. In *AIAA 9th Aerospace Sciences Meeting*.

FAY, J. A. 1969 The spread of oil slicks on a calm sea. In *Oil on the Sea*, pp. 53–63. Springer.

FERNANDEZ, R. L. & IMBERGER, J. 2006 Bed roughness induced entrainment in a high Richardson number underflow. *J. Hydraul. Res.* **44** (6), 725–738.

FLACK, K. A. & SCHULTZ, M. P. 2014 Roughness effects on wall-bounded turbulent flows. *Phys. Fluids* **26** (10), 101305.

FORCHHEIMER, P. 1901 Wasserbewegung durch boden. *Z. Verein. Deutsch. Ing.* **45** (1782), 1788.

FRAGOSO, A. T., PATTERSON, M. D. & WETTLAUFER, J. S. 2013 Mixing in gravity currents. *J. Fluid Mech.* **734**, R2.

GERMANO, M., PIOMELLI, U., MOIN, P. & CABOT, W. H. 1991 A dynamic subgrid-scale eddy viscosity model. *Phys. Fluids* A **3** (7), 1760–1765.

GOLDSTEIN, D., HANDLER, R. & SIROVICH, L. 1993 Modeling a no-slip flow boundary with an external force field. *J. Comput. Phys.* **105** (2), 354–366.

GONZALEZ-JUEZ, E., MEIBURG, E. & CONSTANTINESCU, G. 2009 Gravity currents impinging on bottom-mounted square cylinders: flow fields and associated forces. *J. Fluid Mech.* **631**, 65–102.

GONZALEZ-JUEZ, E., MEIBURG, E., TOKYAY, T. & CONSTANTINESCU, G. 2010 Gravity current flow past a circular cylinder: forces, wall shear stresses and implications for scour. *J. Fluid Mech.* **649**, 69–102.

HACKER, J., LINDEN, P. F. & DALZIEL, S. B. 1996 Mixing in lock-release gravity currents. *Dyn. Atmos. Oceans* **24** (1–4), 183–195.

HÄRTEL, C., MEIBURG, E. & NECKER, F. 2000 Analysis and direct numerical simulation of the flow at a gravity-current head. Part 1. Flow topology and front speed for slip and no-slip boundaries. *J. Fluid Mech.* **418**, 189–212.

HOULT, D. P. 1972 Oil spreading on the sea. *Annu. Rev. Fluid Mech.* **4** (1), 341–368.

HUGHES, G. O. & LINDEN, P. F. 2016 Mixing efficiency in run-down gravity currents. *J. Fluid Mech.* **809**, 691–704.

HUPPERT, H. E. & SIMPSON, J. E. 1980 The slumping of gravity currents. *J. Fluid Mech.* **99** (04), 785–799.

JIMENEZ, J. 2004 Turbulent flows over rough walls. *Annu. Rev. Fluid Mech.* **36**, 173–196.

KEULEGAN, G. 1958 The motion of saline fronts in still water. *Nat. Bur. Stand. Rep.* 5813.

KNELLER, B. C., BENNETT, S. J. & MCCAFFREY, W. D. 1999 Velocity structure, turbulence and fluid stresses in experimental gravity currents. *J. Geophys. Res.* **104** (C3), 5381–5391.

LA ROCCA, M., ADDUCE, C., SCIORTINO, G. & PINZON, A. B. 2008 Experimental and numerical simulation of three-dimensional gravity currents on smooth and rough bottom. *Phys. Fluids* **20** (10), 106603.

https://doi.org/10.1017/jfm.2017.678 Published online by Cambridge University Press

LETTAU, H. 1969 Note on aerodynamic roughness-parameter estimation on the basis of roughness-element description. *J. Appl. Meteorol.* **8** (5), 828–832.

MACDONALD, R. W., GRIFFITHS, R. F. & HALL, D. J. 1998 An improved method for the estimation of surface roughness of obstacle arrays. *Atmos. Environ.* **32** (11), 1857–1864.

MCELWAINE, J. N. 2005 Rotational flow in gravity current heads. *Phil. Trans. R. Soc. Lond.* A **363** (1832), 1603–1623.

MICARD, D., DOSSMANN, Y., GOSTIAUX, L. & VENAILLE, A. 2016 Mixing efficiency in a lock exchange experiment. In *VIIIth International Symposium on Stratified Flows*, vol. 1. University of California.

NEGRETTI, M. E., ZHU, D. Z. & JIRKA, G. H. 2008 The effect of bottom roughness in two-layer flows down a slope. *Dyn. Atmos. Oceans* **45** (1), 46–68.

NIKURADSE, J. 1933 *Laws of Flow in Rough Pipes*. VDI Forschungsheft.

NOGUEIRA, H. I. S., ADDUCE, C., ALVES, E. & FRANCA, M. J. 2014 Dynamics of the head of gravity currents. *Environ. Fluid Mech.* **14** (2), 519–540.

ORLANDI, P. & LEONARDI, S. 2004 Passive scalar in a turbulent channel flow with wall velocity disturbances. *Flow Turbul. Combust.* **72** (2), 181–197.

ORLANDI, P. & LEONARDI, S. 2006 DNS of turbulent channel flows with two- and three-dimensional roughness. *J. Turbul.* **7**, N73.

OTTOLENGHI, L., ADDUCE, C., INGHILESI, R., ARMENIO, V. & ROMAN, F. 2016 Entrainment and mixing in unsteady gravity currents. *J. Hydraul. Res.* **54** (5), 541–557.

ÖZGÖKMEN, T. M. & FISCHER, P. F. 2008 On the role of bottom roughness in overflows. *Ocean Model.* **20** (4), 336–361.

ÖZGÖKMEN, T. M., ILIESCU, T. & FISCHER, P. F. 2009 Large eddy simulation of stratified mixing in a three-dimensional lock-exchange system. *Ocean Model.* **26** (3), 134–155.

PETERS, W. D. & VENART, J. E. S. 2000 Visualization of rough-surface gravity current flows using laser-induced fluorescence. In *9th (Millennium) International Symposium on Flow Visualization*.

PRASTOWO, T., GRIFFITHS, R. W., HUGHES, G. O. & HOGG, A. M. 2009 Effects of topography on the cumulative mixing efficiency in exchange flows. *J. Geophys. Res.* **114** (C8), C08008.

ROTTMAN, J. W. & SIMPSON, J. E. 1983 Gravity currents produced by instantaneous releases of a heavy fluid in a rectangular channel. *J. Fluid Mech.* **135**, 95–110.

SAMASIRI, P. & WOODS, A. W. 2015 Mixing in axisymmetric gravity currents. *J. Fluid Mech.* **782**, R1.

SCHLICHTING, H. 1936 Experimental investigation of the problem of surface roughness. *Ingenieur-Archiv* **7** (1), 1–34.

SCHULTZ, M. P. & FLACK, K. A. 2009 Turbulent boundary layers on a systematically varied rough wall. *Phys. Fluids* **21** (1), 015104.

SHIN, J. O., DALZIEL, S. B. & LINDEN, P. F. 2004 Gravity currents produced by lock exchange. *J. Fluid Mech.* **521**, 1–34.

SIMPSON, J. E. 1972 Effects of the lower boundary on the head of a gravity current. *J. Fluid Mech.* **53** (04), 759–768.

SIMPSON, J. E. 1982 Gravity currents in the laboratory, atmosphere, and ocean. *Annu. Rev. Fluid Mech.* **14** (1), 213–234.

SIMPSON, J. E. & BRITTER, R. E. 1979 The dynamics of the head of a gravity current advancing over a horizontal surface. *J. Fluid Mech.* **94** (03), 477–495.

TANINO, Y. & NEPF, H. M. 2008 Laboratory investigation of mean drag in a random array of rigid, emergent cylinders. *J. Hydraul. Engng* **134** (1), 34–41.

TANINO, Y., NEPF, H. M. & KULIS, P. S. 2005 Gravity currents in aquatic canopies. *Water Resour. Res.* **41** (12), W12402.

THOMAS, L. P., DALZIEL, S. B. & MARINO, B. M. 2003 The structure of the head of an inertial gravity current determined by particle-tracking velocimetry. *Exp. Fluids* **34** (6), 708–716.

TOKYAY, T. & CONSTANTINESCU, G. 2015 The effects of a submerged non-erodible triangular obstacle on bottom propagating gravity currents. *Phys. Fluids* **27** (5), 056601.

https://doi.org/10.1017/jfm.2017.678 Published online by Cambridge University Press

TOKYAY, T., CONSTANTINESCU, G. & MEIBURG, E. 2011 Lock-exchange gravity currents with a high volume of release propagating over a periodic array of obstacles. *J. Fluid Mech.* **672**, 570–605.

TOKYAY, T., CONSTANTINESCU, G. & MEIBURG, E. 2012 Tail structure and bed friction velocity distribution of gravity currents propagating over an array of obstacles. *J. Fluid Mech.* **694**, 252–291.

WILSON, R. I., FRIEDRICH, H. & STEVENS, C. 2017 Turbulent entrainment in sediment-laden flows interacting with an obstacle. *Phys. Fluids* **29** (3), 036603.

WINTERS, K. B., LOMBARD, P. N., RILEY, J. J. & D'ASARO, E. A. 1995 Available potential energy and mixing in density-stratified fluids. *J. Fluid Mech.* **289**, 115–128.

WU, Y. & CHRISTENSEN, K. T. 2010 Spatial structure of a turbulent boundary layer with irregular surface roughness. *J. Fluid Mech.* **655**, 380–418.

YUKSEL OZAN, A., CONSTANTINESCU, G. & HOGG, A. J. 2015 Full-depth lock exchange gravity currents with a high volume of release propagating through arrays of cylinders. *J. Fluid Mech.* **675**, 544–575.

ZGHEIB, N., BONOMETTI, T. & BALACHANDAR, S. 2015 Propagation and deposition of non-circular finite release particle-laden currents. *Phys. Fluids* **27** (8), 086604.

https://doi.org/10.1017/jfm.2017.678 Published online by Cambridge University Press